



**I
N
A
O
E**

Spherically Symmetric Accretion from a Nuclear Young Starburst onto a Super Massive Black Hole

by

Filiberto Hueyotl Zahuantitla

A Dissertation submitted to the Astrophysics
Department in partial fulfillment of the
requirements for the degree of

Ph. D. in Astrophysics

at the

**Instituto Nacional de Astrofísica, Óptica y
Electrónica**

September 2010
Tonantzintla, Puebla

Advisors:

**Dr. Sergiy Silich
Dr. Guillermo Tenorio Tagle, INAOE**

©INAOE 2010



Spherically Symmetric Accretion from a Nuclear
Young Starburst onto a Super Massive Black Hole

by

Filiberto Hueyotl Zahuantitla

A Dissertation

Submitted to the Astrophysics Department

in partial fulfillment of the requirements for the degree of

Ph. D. in Astrophysics

at the

Instituto Nacional de Astrofísica, Óptica y Electrónica

Tonantzintla, Puebla

Advisors:

Dr. Sergiy Silich

Dr. Guillermo Tenorio Tagle

©INAOE

September 24, 2010

1	Introduction	1
2	The hydrodynamic model	10
2.1	Input physics	11
2.2	Main hydrodynamic equations	13
2.3	The semi-analytic approach	14
2.4	Numerical simulations	17
3	Extreme positive star-formation feedback in young as-	
	sembling galaxies	20
3.1	Introduction: SCUBA galaxies	20
3.2	Star formation under a large SFR	22
3.3	The three hydrodynamic regimes	26
3.3.1	The supergalactic wind solution	28
3.3.2	The bimodal hydrodynamic solution	32
3.3.3	The gravitationally bound solution	35
3.4	Discussion	41

3.5	Conclusions	44
4	The hydrodynamic interplay between SMBHs and nuclear starbursts	46
4.1	Introduction: the nuclear starburst-SMBH interplay . . .	46
4.2	Bimodal solution in the quasi-adiabatic regime	49
4.2.1	Boundary conditions and the appropriate solution	50
4.3	The bimodal solution in the catastrophic cooling regime .	57
4.3.1	Initial conditions for the simulations	59
4.3.2	Tests of the numerical simulations	61
4.3.3	The numerical solution above the threshold energy	63
4.3.4	The structure of the bimodal flow in the catastrophic cooling regime	66
4.3.5	Impact of the supermassive black hole mass on the bimodal flow	70
4.3.6	Impact of the minimum temperature allowed on the accretion flow	71
4.4	The bimodal flow in the gravitationally bound regime . .	73
4.5	The SMBH accretion rate and luminosity, and the power of the NSB super wind	77
4.6	X-ray emission from the accretion flow	84
4.7	Conclusions	85
5	Conclusions	88

6	Physics to be considered in future projects	92
A	The Eulerian hydro-code ZEUS	96
B	Impact of the inner grid boundary on the simulations	99

Chapter 1

Introduction

The present dissertation study the hydrodynamics of the reinserted matter by the massive members of compact and massive star-formation regions by taking into account the major physics involved in the problem, i.e, sources of mass and energy, radiative losses of the thermalized plasma and the gravity pull of the system. This thesis is divided in two parts: the first part presents a study of the hydrodynamics of the injected matter by massive and violent star-forming events similar to those detected in high redshift submillimeter galaxies. The second part is devoted to one of the most challenge problems in modern astrophysics: the interplay between nuclear star-formation activity and the supermassive black holes detected in the nuclear regions of galaxies with different levels of nuclear activity. The theory here presented can be scaled to systems of different sizes and masses, and the only difference between the two parts mentioned above is that the former considers only the gravity pull from the dynamical mass of the star-forming region while

in the second one the gravitational potential from both the stellar component and the super massive black hole are considered, which makes the solution different. The hydrodynamic solutions in the case of a young assembling galaxy with high star formation rates and in case of a nuclear starburst feeding a super massive black hole, depend on many parameters, here however, we understand that in both cases there are three possible hydrodynamic solutions: the quasi-adiabatic, the catastrophic cooling and the gravitationally bound regimes. Which of these three possibilities take place depends on where the system is located in the parameter space defined by the mechanical luminosity (or star formation rate in case of young assembling galaxies) of the star-forming region, the mass of the starburst and its size, and additionally on the mass of the super massive black hole in the case of nuclear starbursts with a central black hole. It is shown that the major players which define the type of solution are the radiative cooling and the gravity pull of the system.

Here, Chapter 2 contains the input physics to model the star-forming region (an assembling galaxy or a nuclear starburst) and the set of hydrodynamic equations used in this work. Two methods are used to integrate the conservation equations: a semi-analytic approach used mainly in the quasi-adiabatic regime, and full numerical simulations used to find the solution in the catastrophic cooling and the gravitationally bound regimes. Both methods are described in Chapter

2. The study of star-formation feedback in young assembling galaxies with extreme star-formation rates is presented in Chapter 3. Chapter 4 presents a detailed study of the hydrodynamics of the matter reinserted by nuclear starbursts in presence of a central supermassive black hole. In Chapter 5 are the conclusions of this thesis. And finally, Chapter 6 outlines some key points that will be considered in future projects in order to improve the models here presented.

Part I

In cosmology today the study of star formation negative feedback is recognized as one of the central issues regarding galaxy formation (Deckel & Silk 1986); Frianca & Terlevich 1998; Tutukov et al. 2000; Scannapieco et al. 2002; Ferreras et al. 2002). The large UV photon output from massive stars and their violently deposited mechanical energy make them indeed major players in the dynamics of the interstellar matter (ISM) and key negative feedback agents able to limit and stop star formation defining the efficiency of the process (see Tenorio-Tagle & Bodenheimer 1988, Elmegreen 1999 and references therein). However, as shown by Tenorio-Tagle et al. (2005, 2007) and Wünsch et al. (2008) for the case of massive and compact super stellar clusters, this may not be the whole story as the stellar feedback may, in extreme cases, become positive. This would allow gravity to win over thermal pressure. This may also be the case if one considers star forma-

tion in the Submillimeter Common-User Bolometric Array (SCUBA) galaxies—high redshift sources with highest ($\sim 1000 M_{\odot} \text{ yr}^{-1}$) star formation rates (SFRs) known so far. These have been observed in the submillimeter continuum (emission from warm dust in the rest-frame far-IR/submillimeter wavelengths), in the CO line emission associated with the cold molecular gas, and in the near-infrared integral field spectroscopy, which deals with the rest-frame optical emission lines associated with the photoionized gas (see, for example, Hughes et al. 1998; Greve et al. 2005; Tacconi et al. 2006, 2008; Swinbank et al. 2006, and references therein).

The global properties of SCUBA galaxies include a typical dynamical mass of $5 \pm 3 \times 10^{11} M_{\odot}$, a gas to dynamical mass fraction, $f_g = M_{gas}/M_{dyn} \sim 0.25\text{--}0.3$, and a radius of about 1–3 kpc, parameters consistent with the expected properties of massive spheroids in the early universe (Greve et al. 2005; Swinbank et al. 2006; Tacconi et al. 2006, 2008; Schinnerer et al. 2008). The long star formation duty cycle with a time scale $\sim 100\text{--}300$ Myr and the in-homogeneous nature of SCUBA sources favor a continuous star formation scenario (Swinbank et al. 2006; Tacconi et al. 2008). In Chapter 3 it is shown how massive and violent star-forming events driven by a high rate of star formation lead to positive feedback. Looking at some extreme cases, one can identify radiative cooling as the agent capable of downgrading the impact of the stellar energy deposition, leading inevitably to an extreme

positive star formation feedback condition which should play a major role in galaxy formation. There it is also shown that gravity is another major player. The gravitational pull of the galaxy also leads to a positive feedback condition, particularly in compact protogalactic sources. The gravitational pull then prevents the formation of a supergalactic wind, retaining the injected and ablated matter within the star-forming region, favoring its accumulation and conversion into future generation of stars. The results of this part of the dissertation are published in the paper “On the extreme positive star formation feedback condition in SCUBA sources” (Silich et al. 2010).

Part II

Powerful starbursts have been conclusively detected in the nuclear regions of galaxies with active galactic nuclei (AGN; see for a review Veilleux et al. 2005 and Heckman 2008). These include quasars (Hao et al. 2005; 2008), Seyferts (Imanishi et al. 2003; Davies et al. 2007; Watabe et al. 2008; Chen et al. 2009), submillimeter galaxies with an extreme star formation rate (Alexander et al. 2005, Walter et al. 2009) and even low luminosity AGNs (Cid Fernandes & Terlevich 1995; González-Delgado et al. 2004). Such nuclear starbursts (NSBs) have compact sizes <100 pc and masses ranging from $10^6 - 10^9 M_{\odot}$ (Davies et al. 2007; Watabe et al. 2008) and may have complicated star formation histories with several episodes of star formation (Walcher et

al. 2006). Some of them with a complex history of star formation are found in a number of nearby spiral (Rossa et al. 2006) and elliptical galaxies (Wehner & Harris, 2006; Côté et al. 2006).

Some NSBs have been found to coexist with supermassive black holes (SMBHs) (e.g., Filippenko and Ho 2003; González Delgado et al. 2008; Seth et al. 2008a; Kormendy et al. 2009). Ferrarese et al. (2006) claimed that massive galaxies ($M_{gal} > 10^{10} M_{\odot}$) host SMBHs whereas less massive galaxies host only nuclear clusters. A similar conclusion was found by Graham & Spitler (2009) in a study based on a compilation of the cases of coexisting nuclear clusters and SMBHs with reliably estimated masses, they show that the masses of the nuclei of the most massive elliptical galaxies appear to be dominated by SMBHs, with nuclear stellar clusters not detected in many cases. The nuclear masses of the least massive spheroids appear to be dominated, however, by the masses of their respective nuclear star clusters. More intriguing is the realization that nuclear stellar clusters appear to obey similar scaling relationships with properties of their host galaxy as do SMBHs, like for example, the $M_{SMBH} - \sigma$ or $M_{SMBH} - M_{bulge}$ relations (Rossa et al. 2006; Wehner & Harris 2006; Ferrarese et al. 2006; Graham & Spitler 2009). King (2003, 2005) try to explain the $M_{SMBH} - \sigma$ relation by assuming that the black hole accretes at the Eddington ratio. However, Kormendy et al. (2009) argue that this apparent relation could be an accident and that there is no further relation between

massive black holes and nuclear star clusters than that both are fed by gas from the surrounding galactic disc. In fact there are many efforts to try to understand what happens at the nuclear regions of galaxies with SMBHs by performing 1D, 2D and 3D calculation with several simplifications and assumptions. For example, Yuan & De-Fu-Bu (2010) performed 2D hydrodynamic simulations of hot accretion flows and they consider only Bremsstrahlung cooling without sources of mass and energy while Hobbs et al. (2010) performed simulations of gas accreting onto a SMBH immersed into an isothermal, static spherical bulge potential ($r < 100\text{pc}$). In fact, even basic issues regarding, for example, the impact of type II supernovae (SN) on the matter left over from star formation, seem to be still undecided. One can find in the literature massive starbursts with a SN rate of 1 yr^{-1} structuring a gaseous disk of just $10^7 M_{\odot}$ (Wada & Norman 2002) while other calculations assume that type II supernova might evacuate most of the nuclear region from gas and dust (Shartmann et al. 2009) and have considered only the evolution after the last type II SN explosion.

The physical connection between nuclear starbursts and super massive black holes remains as one of the central issues in the theory of AGN galaxies to understand for example, the strong correlation between the AGN activity and star-formation rates in the nuclear region (Davies et al. 2007; Chen et al. 2009), the process of cosmological growth of SMBHs (Lípari & Terlevich, 2006; Booth & Schaye, 2009) and their

co-evolution with the bulges of their host galaxies (Begelman & Nath, 2005; Di Matteo et al. 2005; Somerville et al. 2008), and the delay between the starburst and the black hole activity (Davies et al. 2007; Ciotti et al. 2009). Thus, in order to understand the interplay between nuclear starburst and the central supermassive black hole, this dissertation presents in Chapter 4 a comprehensive, spherically symmetric solution for the gaseous flow around a SMBH at the center of young (< 40 Myr) starbursts regions. The hydrodynamic solution depends, as in the case of young assembling galaxies presented in Chapter 3, on where the system is located in the parameter space defined by the size and mass of the nuclear starburst and the mass of the central supermassive black hole. However, in this case the solution is always bimodal with an accretion flow formed inside the stagnation radius and a starburst wind flow promoted by the high pressure of the thermalized plasma in the zone between the stagnation point and the starburst edge. The bimodal solution could be in the quasi-adiabatic regime with small values of the stagnation radius and small accretion rates or in the catastrophic cooling regime with large stagnation radius and high accretion rates. In the gravitationally bound regime the stationary solution does not exist and eventually all the reinserted matter by the starburst falls towards the central super massive black hole. The results of this part of the dissertation are published in two papers “Spherically symmetric accretion onto a black hole at the center of a young stellar cluster” (Silich et al.

2008) and “On the hydrodynamic interplay between a young nuclear starburst and a central supermassive black hole” (Hueyotl-Zahuantitla et al. 2010).

Chapter 2

The hydrodynamic model

This chapter presents the input physics and main equations used in this work to find the hydrodynamic solution of the reinserted matter by massive stars in young assembling galaxies with extreme star-formation rates (Chapter 3), and in the case of young nuclear starbursts fueling super massive black holes with the matter left over via stellar winds and supernovae (Chapter 4). Both problems depend on multiple parameters and thus “some” assumptions and simplifications are needed in order to handle them. Here, section 2.1 presents the main physics and assumptions considered in this work. Section 2.2 presents the complete hydrodynamic equations and a description of all parameters here used. The set of equations solved in the semi-analytic approach is given in section 2.3. The algorithm used to include all physics here considered into the numerical simulations is presented in section 2.4.

2.1 Input physics

The model consist (in both cases) on a spherically symmetric starburst with homogeneous distribution of the stellar component¹. In Chapter 3 a continuous star formation is assumed whereas in Chapter 4 an instantaneous starburst is considered. Nevertheless, the main hydrodynamic equations are the same in both chapters, with small differences indicated in the text. It is assumed full thermalization of the kinetic energy via random collisions of the mass supplied by stellar winds and supernovae within the star-forming region (Chevalier & Clegg 1985). The model accounts for radiative losses of the thermalized matter (Silich et al. 2003, 2004; Tenorio-Tagle et al. 2005, 2007, Wünsch et al. 2008) and also for the gravity pull from the system (Silich et al. 2008, 2010; Hueyotl-Zahuantitla et al. 2010). Here we understand that these two physical processes determine the hydrodynamic solution of the reinserted gas: the quasi adiabatic, the catastrophic cooling, or the gravitationally bound solutions. In the case of Chapter 3 the gravitational well from the star-forming region is considered, and the gravity pull from both the starburst and the central black hole is accounted in Chapter 4. The self gravity from the reinserted gas is neglected. Following Nulsen & Fabian (2000) and Ciotti et al. (2009), it is assumed that the angular

¹Note that the terms *starburst* or *star-forming region* is used to refer to a young assembling galaxy in the case of Chapter 3, whereas they are used for a nuclear star formation region in the case of Chapter 4.

momentum of the thermalized gas is not too large and thus this thesis presents only the one-dimensional solution. The mass and energy are deposited uniformly inside the starburst volume, therefore the results here presented may resemble to more sophisticated 2D and 3D models, see for example the bimodal solution presented by Tenorio-Tagle et al. (2007) and Wünsch et al. (2008) for 1D and 2D calculations, respectively, in the case of very compact and massive star clusters without accounting for the gravity pull. Here it is assumed that the parameters of the system do not change with time. In the case of Chapter 4 the feedback provided by the central SMBH (Silk & Rees 1998; Ciotti & Ostriker 2001; Ciotti et al. 2009, 2010) is not considered.

The set of the hydrodynamic equations are solved using two methods: the semi-analytic approach (Silich et al. 2008) used mainly in the quasi-adiabatic regime, and full numerical simulations (Hueyotl-Zahuantitla et al. 2010) used to find the complete solution in the catastrophic cooling and the gravitationally bound regimes. The semi-analytic method is used to find the limits of such regimes and to estimate the stagnation radius even in the case when the catastrophic cooling sets in.

2.2 Main hydrodynamic equations

The full hydrodynamic equations used through this work for a spherically symmetric flows that results from the energy and mass deposition within young and massive starbursts with radius R , mass M , and mechanical luminosity L , subject to the gravitational potential ϕ , are the mass, momentum and energy conservation equations²:

$$\frac{\partial \rho}{\partial t} + \nabla \cdot (\rho u) = q_m, \quad (2.1)$$

$$\frac{\partial u}{\partial t} + (u \cdot \nabla)u = -\nabla P/\rho - q_m u/\rho - \nabla \phi, \quad (2.2)$$

$$\frac{\partial E}{\partial t} + \nabla \cdot (E + P)u = q_e - Q - \rho u \nabla \phi, \quad (2.3)$$

where, the quantities P , u , and ρ in equations [2.1]-[2.3] are the thermal pressure, the velocity, and the density of the thermalized matter, respectively. Note that $E = \rho\lambda$, is the total energy per unit volume of the thermalized gas, where $\lambda = \epsilon + u^2/2$ and ϵ are the total and the internal energy per unit mass, respectively. Therefore, the internal energy per unit volume is $e \equiv \rho\epsilon = P/(\gamma - 1)$. The mass and energy deposition rates per unit volume, $q_m = 3\dot{M}/4\pi R^3$ and $q_e = 3L/4\pi R^3$, are assumed to be spatially constant inside the star cluster and equal to zero if $r > R$. The mechanical luminosity, L , relates to the total

²Note that in Chapters 3 the suffix ‘‘SF’’ is used to indicate the parameters of the star-forming region whereas in Chapter 4 the suffix ‘‘NSB’’ is used to refer to the parameters of the nuclear starburst.

mass deposition rate according to $L = \dot{M}V_{A,\infty}^2/2$, where $V_{A,\infty}$ is the adiabatic terminal speed. The mechanical luminosity is scaled accordingly to account for a continuous star formation (Chapter 3) or an instantaneous burst (Chapter 4). Here $Q = n_e n_i \Lambda(T, Z)$ is the cooling rate, n_e and n_i are the electron and ion number densities, and $\Lambda(T, Z)$ is the Raymond & Cox cooling function tabulated by Plewa (1995), which depends on the thermalized gas temperature, T , and metallicity, Z . The gravity force is $-\nabla\phi = -GM_*/r^2$, where M_* is the mass enclosed within a sphere of radius r . Here, in the more general case $M_* = M_{SMBH} + M(r/R)^3$, if $r \leq R$, and $M_* = M_{SMBH} + M$, if $r > R$, when the mass of the central super massive black hole, M_{SMBH} , is considered. Thus in order to find the hydrodynamic solution one has to know the mechanical luminosity and mass deposition rate from the starburst, its radius and the total mass of the system.

2.3 The semi-analytic approach

The semi-analytic model uses the set of equation [2.1]-[2.3], avoiding time derivatives. In spherical coordinates the set of the hydrodynamic conservation equations are (see Holzer & Axford 1970)

$$\frac{1}{r^2} \frac{d}{dr} (\rho u r^2) = q_m, \quad (2.4)$$

$$\rho u \frac{du}{dr} = -\frac{dP}{dr} - q_m u - \frac{G\rho M_*}{r^2}, \quad (2.5)$$

$$\frac{1}{r^2} \frac{d}{dr} \left[\rho u r^2 \left(\frac{u^2}{2} + \frac{\gamma}{\gamma-1} \frac{P}{\rho} \right) \right] = q_e - Q - \frac{G\rho u M_*}{r^2}. \quad (2.6)$$

Note that the set of equations [2.4]-[2.6] are valid in the region inside the starburst volume. Outside the cluster volume $q_m = q_e = 0$. One can easily integrate the mass conservation equation both inside and outside the cluster volume and then rewrite the set of equations [2.4]-[2.6] in the form

$$\rho = \frac{q_m r}{3u} \left(1 - \frac{R_{st}^3}{r^3} \right) \quad (2.7)$$

$$\frac{dP}{dr} = -\rho u \frac{du}{dr} - q_m u - \frac{G\rho M_*}{r^2} \quad (2.8)$$

$$\frac{du}{dr} = \frac{(\gamma-1)(q_e - Q) + q_m \left[\frac{\gamma+1}{2} u^2 - \frac{2}{3} \left(1 - \frac{R_{st}^3}{r^3} \right) \left(c_s^2 - \frac{V_e^2}{4} \right) \right]}{\rho(c_s^2 - u^2)}, \quad (2.9)$$

within the cluster volume, $r \leq R$, where the constant in the integral form of the mass conservation equation is not equal to zero. In this case it depends on the value of the stagnation radius, R_{st} , then the integration constant is $C = -q_m R_{st}^3/3$, because at the stagnation point the flow velocity is zero, $u = 0$. In the region outside the cluster volume, $r > R$, the set of equations are

$$\rho = \frac{\dot{M}}{4\pi u r^2}, \quad (2.10)$$

$$\frac{dP}{dr} = -\frac{\dot{M}}{4\pi r^2} \frac{du}{dr} - \frac{G\dot{M}M_*}{4\pi u r^4} = -\frac{\dot{M}}{4\pi r^2} \left(\frac{du}{dr} + \frac{V_e^2}{2ur} \right), \quad (2.11)$$

$$\frac{du}{dr} = \frac{2u}{r} \frac{2\pi(\gamma-1)Qr^3/\dot{M} + c_s^2 - V_e^2/4}{u^2 - c_s^2}. \quad (2.12)$$

Here $c_s = (\gamma P/\rho)^{1/2}$ is the sound speed in the hot thermalized ejecta, and we define $V_e \equiv (2GM_*/r)^{1/2}$, which is equal to the escape velocity for $r > R$.

Note that the inclusion of gravity terms does not affect the relation between the gas number density and the temperature at the stagnation point found in Silich et al. (2004):

$$n_{st} = q_m^{1/2} \left[\frac{V_{A,\infty}^2/2 - c_{st}^2/(\gamma - 1)}{\Lambda(Z, T_{st})} \right]^{1/2}, \quad (2.13)$$

where $V_{A,\infty} = (2q_e/q_m)^{1/2}$ is the adiabatic wind terminal speed, c_{st} and $\Lambda(Z, T_{st})$ are the sound speed and the cooling function calculated at $r = R_{st}$. One can prove this relation by comparing the derivative of the velocity at the stagnation point obtained from equation [2.9] with that obtained from equation [2.7] and requiring a finite derivative of density at the stagnation point. Note that Sarazin & White (1987) obtained a similar relation from the energy conservation equation in their cooling flow model. Equation [2.13] is used to estimate the pressure at the stagnation radius for models at the threshold energy which separates the quasi-adiabatic solution from catastrophic cooling regime, and is used to estimate the value of the stagnation radius in the case of catastrophic cooling regime, where full numerical simulations are required in order to find the complete solution, see Tenorio-Tagle et al. (2007).

2.4 Numerical simulations

The numerical approach is based on the finite difference Eulerian hydrodynamic code ZEUS-3D v.3.4.2 (Stone & Norman 1992), which solves the time dependent hydrodynamic equations [2.1]-[2.3] using the operator splitting method, see Appendix A. Following Tenorio-Tagle et al. (2007) and Wünsch et al. (2008), the mass and energy deposition rates per unit volume, q_m and q_e , respectively, are added at each time step, to the computed density and total energy in every cell, ρ_{old} and $e_{tot,old}$, respectively, when located inside the starburst volume: $\rho_{new} = \rho_{old} + q_m dt$, and the velocity is corrected so that the momentum is conserved, $v_{mid} = v_{old} \rho_{old} / \rho_{new}$; the internal energy is corrected to conserve the total energy, $e_{i,mid} = e_{tot,old} - \rho_{new} v_{mid}^2 / 2$, and the new energy is inserted as a form of internal energy $e_{i,new} = e_{i,mid} + q_e dt$ (Tenorio-Tagle et al. 2007 and Wünsch et al. 2008). In this work the velocity of the flow at each radius is updated according to $v_{new} = v_{mid} + a_g dt$, where $a_g = -GM_*/r^2$ is the gravitational acceleration at each radius.

The cooling routine accounts for extremely fast cooling (Tenorio-Tagle et al. 2007; Wünsch et al. 2008) both inside and outside the star cluster volume. The change of internal energy, e , due to cooling is

$$\left(\frac{de}{dt}\right)_{cool} = -n^2 \Lambda(T, Z), \quad (2.14)$$

where it was assumed that $n_i = n_e$. The gas number density is computed according to $n = \rho / (\mu m_p)$, where m_p is the proton mass and

$\mu = 0.609$ is the mean mass per particle. The right-hand side of equation [2.14] is evaluated in the middle of time steps to maintain the second-order accuracy of the code and is considered in the computation of the time step, see Wunsch et al. (2008): the amount of energy that can be radiated from a given cell during one time step must be less than 10% of its internal energy, then the time step is decreased to meet this condition, but since this could lead to extremely small time steps, which could substantially degrade the overall code performance, then it is not allowed the *global* time step to decrease below 0.1 times the “hydrodynamic” time step determined by the Courant-Friedrich-Levi criterion. If a certain cell requires an even smaller time step due to the fast cooling rate condition, the time step is subdivided even more. Using such small-enough sub-steps, the energy equation is integrated only in the affected cells. Note that this time refinement is applied only locally.

In order to simulate the effect of the stellar UV radiation field, in most of the simulations it is not allowed the gas temperature to drop below $T_{min} = 10^4$ K. This is equivalent to the assumption that there are sufficient UV photons to ionize the dense thermal unstable matter, which otherwise would cool to much lower temperatures and may become gravitationally unstable. All simulations here presented have been carried out in spherical coordinates with symmetry along the θ and ϕ -coordinates. The computational domain extends over the inter-

val (R_{in}, R_{out}) , where $0 < R_{in} \ll R_{NSB} < R_{out}$. A uniform grid in the radial direction was used, with open boundary condition at the inner and outer zones, which allows the gas to escape from the computational domain.

Chapter 3

Extreme positive star-formation feedback in young assembling galaxies

3.1 Introduction: SCUBA galaxies

This chapter presents a detailed study of the hydrodynamics of the matter reinserted by massive stars via stellar winds and supernovae explosions in young assembling galaxies. Here it is shown that the interplay between the thermalization of the kinetic energy provided by massive stars, radiative cooling of the thermalized plasma, and the gravitational pull of the host galaxy lead to three different hydrodynamic regimes. These are: (1) the quasi-adiabatic supergalactic wind; (2) the bimodal flows, with mass accumulation in the central zones and gas expulsion from the outer zones of the assembling galaxy; and (3)

the gravitational bound regime, for which all of the gas returned by massive stars remains bound to the host galaxy and is likely to be re-processed into further generation of stars. Which of the three possible solutions takes place depends on the mass of the star-forming region, its mechanical luminosity (or star formation rate), and its size. The model predicts that massive assembling galaxies with large star formation rates similar to those detected in Submillimeter Common-User Bolometric Array sources (SCUBA sources with high star-formation rates $\sim 1000 M_{\odot} \text{yr}^{-1}$) are likely to evolve in a positive star formation feedback condition, either in the bimodal or in the gravitationally bound regime. This implies that star formation in these sources may have little impact on the intergalactic medium and results instead into a fast interstellar matter enrichment, as observed in high redshift quasars. In section 3.2, we examine the physical implications of massive star-formation rates (SFRs). The analysis of the physical properties of the various possible hydrodynamic regimes is given in section 3.3. The implications of events with a high SFR and our conclusions are given in Sections 3.4 and 3.5, respectively. The main results of this chapter are published in Silich et al. (2010).

3.2 Star formation under a large SFR

If one scales the evolutionary synthesis models (e.g., Leitherer & Heckman 1995) for star clusters generated by a constant SFR to the values inferred from the SCUBA sources ($\geq 100 M_{\odot} \text{ yr}^{-1}$; e.g., Greve et al. 2005; Swinbank et al. 2006; Tacconi et al. 2006), one sees that as a result of the continuous death and creation of massive stars, the UV photon output will level off at $\sim 10^{55}$ ionizing photons s^{-1} after 3 Myr of the evolution. The mechanical energy deposited by the evolving stars (L_{SF}) through winds and supernovae (SNe) will also increase, although not so rapidly, to reach a constant value $\sim 2.5 \times 10^{43}$ erg s^{-1} after 40 Myr of evolution. Accordingly, the mass violently returned to the ISM by stellar winds and supernovae will amount to $3 \times 10^7 M_{\odot}$ after 10 Myr, reaching almost $10^9 M_{\odot}$ after 100 Myr of evolution. The absolute values of all the above-mentioned variables ought to be linearly scaled by more than an order of magnitude, at the given times, if instead of a SFR equal to $100 M_{\odot} \text{ yr}^{-1}$, one assumes the even larger values inferred for the most powerful SCUBA sources ($\geq 1000 M_{\odot} \text{ yr}^{-1}$).

At first glance, such an energy deposition and such a vast amount of matter so violently injected would unavoidably lead to extreme massive outflows into the intergalactic medium (see, e.g., Heckman et al. 1990; Strickland & Stevens 2000; Scannapieco et al. 2002; Tenorio-Tagle et al. 2003; Veilleux et al. 2005, and references therein). Supergalactic winds

are believed to result from the full thermalization of the kinetic energy of the ejecta through multiple random collisions within the star-forming volume (see Chevalier & Clegg 1985). Thermalization generates the large over-pressure that continuously accelerates the deposited matter to finally blow it out of the star-forming volume, composing a stationary superwind with an adiabatic terminal speed $V_{A,\infty} = (2L_{SF}/\dot{M}_{SF})^{1/2}$, where L_{SF} and \dot{M}_{SF} are the mechanical energy and mass deposition rates provided by stellar winds and supernovae explosions within the star-forming volume. For this to happen, the ejecta has to reach an outward velocity equal to the sound speed right at the star-forming boundary, R_{SF} , to then fulfill the stationary condition in which the rate at which matter is deposited equals the rate at which it streams away from the star-forming region: $\dot{M}_{SF} = 4\pi R_{SF}^2 \rho_{SF} c_{SF}$, where ρ_{SF} and c_{SF} are the values of density and sound speed at the surface of the star-forming region. However, as shown in the series of papers Silich et al. (2003, 2004), Tenorio-Tagle et al. (2005, 2007) and Wünsch et al. (2008), when dealing with the outflows generated by massive bursts of star formation, the impact of radiative cooling becomes a relevant property, as is gravity, able to hold a fraction of the deposited matter within the star cluster volume.

In the case of an instantaneous burst of star formation, stellar winds and supernovae are able to remove the matter left over from star formation out of the star cluster volume in just a few megayears (Melioli & de

Gouveia Dal Pino 2006; Tenorio-Tagle et al. 2006), and so the hydrodynamic solution considers only the matter reinserted by the massive stars. In the continuous star formation scenario, however, a gas reservoir out of which a constant SFR could be sustained is required. This implies that besides the mass returned by supernovae and stellar winds, \dot{M}_{SF} , the flow may hold additional matter. This results from the destruction and mass ablation from star-forming region: $\dot{M}_{ld} = \eta_{ld} SFR$, where η_{ld} is the mass loading coefficient. The total mass input rate into the flow is then

$$\dot{M} = \dot{M}_{SF} + \dot{M}_{ld} = \left(\frac{2L_0}{V_{A,\infty}^2} + \eta_{ld} \times 1 \text{ M}_\odot \text{ yr}^{-1} \right) \frac{SFR}{1 \text{ M}_\odot \text{ yr}^{-1}}, \quad (3.1)$$

where L_0 is the normalization coefficient, which relates the mechanical energy output rate, L_{SF} , to the SFR:

$$L_{SF} = L_0 (SFR/1 \text{ M}_\odot \text{ yr}^{-1}). \quad (3.2)$$

Hereafter we shall adopt $L_0 = 2.5 \times 10^{41} \text{ erg s}^{-1}$ and $V_{A,\infty} = 2750 \text{ km s}^{-1}$. These values result from Starburst 99 synthetic models for a continuous star formation mode with a Salpeter IMF and sources between 0.1 M_\odot and 100 M_\odot , for ages $t \geq 40 \text{ Myr}$ (Leitherer et al. 1999). Note that mass loading changes the outflow terminal speed, which in this case is smaller than $V_{A,\infty}$:

$$V_\infty = \left(\frac{2L_{SF}}{\dot{M}_{SF} + \dot{M}_{ld}} \right)^{1/2} = \frac{V_{A,\infty}}{\left(1 + \frac{1 \text{ M}_\odot \text{ yr}^{-1} \eta_{ld} V_{A,\infty}^2}{2L_0} \right)^{1/2}} \quad (3.3)$$

The hydrodynamic equations here used include the gravitational pull from the dynamical mass which is assumed to be homogeneously distributed inside the star forming region, see Chapter 2. For the calculations, our semi-analytic stationary wind code (Silich et al. 2008) and the hydro-code ZEUS3D (Stone & Norman 1992) modified to account for fast radiative cooling (Tenorio-Tagle et al. 2007 and Wünsch et al. 2008) and modified in this work to account for the gravity pull of the system were used.

In our approach, it is also assumed that the mass of the flow is negligible compared to the dynamical mass of the system, and thus the self-gravity of the reinserted gas is not included in the calculations. For example, the mass of the flow within the star-forming region, M_{flow} , normalized to the dynamical mass of the system is $M_{flow}/M_{dyn} \approx 2 \times 10^{-5}$ and $M_{flow}/M_{dyn} \approx 8 \times 10^{-3}$ in the case of model 1 with a low SFR and model 4 with a high SFR, respectively. As mentioned in Chapter 2, to obtain the stationary hydrodynamic solution one has to know the mechanical luminosity and mass deposition rates, which in this chapter are defined by equations [3.1] and [3.2], and the radius of the star forming region, R_{SF} . We use the equilibrium cooling function, $\Lambda(T, Z)$, tabulated by Plewa (1995) and set the metallicity of the plasma to the solar value in all calculations. Our reference models are presented in Table 3.1. Here Column 1 marks the model in our list, the ablation coefficient, η_{ld} , is presented in Column 2, Columns 3, 4 and 5 present

the radius, dynamical mass of the star-forming region, and the SFR, respectively. Column 6 provides information regarding the resultant hydrodynamic regime.

Table 3.1: Reference models

Model	η_{ld}	Radius (kpc)	Dynamical mass ($10^{11} M_{\odot}$)	SFR ($M_{\odot} \text{ yr}^{-1}$)	Regime
(1)	(2)	(3)	(4)	(5)	(6)
1	0.5	2.5	2	2	Superwind
2	0.5	1.65	2	2	Superwind
3	0.5	1.2	2	2	Grav. Bound
4	0.5	2.5	2	1200	Bimodal
5	0.5	1.7	2	1200	Bimodal
6	0.5	1.2	2	1200	Grav. Bound

3.3 The three hydrodynamic regimes

There are three major hydrodynamic regimes that develop within galaxies undergoing a large SFR. Which of the three possible solutions takes place depends on the mass of the star-forming region and its position in the mechanical luminosity or SFR versus size (R_{SF}) parameter space. Figure 3.1 presents the threshold lines, which separates pro-

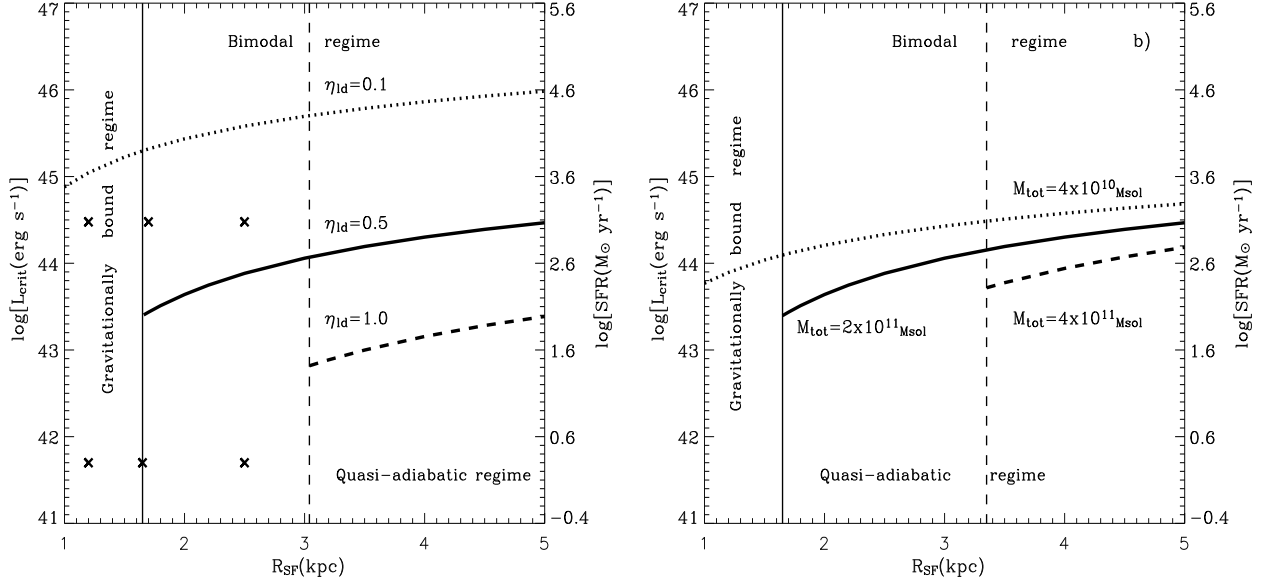


Figure 3.1: Threshold SFR or energy input rate versus the threshold size. The left panel displays the threshold mechanical luminosity, SFR and critical radii for different values of η_{ld} in the case when the dynamical mass in the star forming system equals to $M_{dyn} = 2 \times 10^{11} M_{\odot}$. The limiting energy input rate and its corresponding constant star formation rate (right-hand axis) above which strong radiative cooling inhibits the stationary superwind solution, as a function of the size of the star-forming region and the mass ablation coefficient, η_{ld} . These are terminated at the vertical lines, which display the critical radii, R_{crit} . Gravity inhibits the formation of supergalactic winds in systems with smaller radii. The right hand panel shows how the location of the threshold lines depends on the total mass of the star forming region. Several of the cases here presented are marked by crosses in the left panel. Note that the vertical lines that marks the critical radius (R_{crit}) for $\eta_{ld} = 0.1$ in the left panel, and for $M_{dyn} = 4 \times 10^{10} M_{\odot}$, in the right panel, lie within 1 kpc and thus are not shown.

togalaxies evolving in different hydrodynamic regimes. The left panel presents threshold lines for protogalaxies whose dynamical mass is equal to $2 \times 10^{11} M_{\odot}$ for different values of the ablation coefficient ($\eta_d = 0.1$, 0.5 and 1.0, dotted, solid, and dashed lines, respectively). Below the threshold lines, radiative cooling has a negligible effect on the flow and the reinserted matter ends up as a superwind. Above these lines, radiative cooling leads to a bimodal regime in which some of the reinserted matter within the densest central regions loss its pressure and is unable to participate in the galactic wind. Instead, it accumulates there, fueling further stellar generations (Tenorio-Tagle et al. 2005; Wunsch et al. 2008). For compact star-forming regions, to the left of the vertical lines shown in Figure 3.1 ($R_{SFR} < R_{crit}$) gravity inhibits the formation of a super wind, leading instead to matter accumulation and to further generations of star formation. In these cases, the sound speed at the surface of the star-forming region is smaller than $\sim (GM_{dyn}/2R_{SF})^{1/2}$, which is one half of the escape speed from the protogalaxy surface. The threshold lines for less ($4 \times 10^{10} M_{\odot}$) and more ($4 \times 10^{11} M_{\odot}$) massive galaxies with $\eta_d = 0.5$ are presented in Figure 3.1, right-hand panel.

3.3.1 The supergalactic wind solution

Figure 3.1 shows that there is a large fraction of the parameter space that leads to a stationary supersonic winds. In these cases, all the deposited matter, as well as that ablated from clouds, is able to escape

from the gravitational well of the galaxy. For this to happen, the flow has its stagnation point (the point where the velocity of the flow is equal to zero) right at the center of the galaxy ($R_{st} = 0$ pc) and its sonic point at the surface. The matter accelerates then through pressure gradients to reach supersonic velocities and form a supergalactic wind as it streams away from the galaxy.

Models 1 and 2 in Table 3.1 undergo such supergalactic winds. The distribution of the hydrodynamic variables in these cases are shown in Figure 3.2. Here, panel (a) presents the flow velocity (solid line) in the case of model 1 and compares this to the local sound speed (dashed line) and the escape velocity (dotted line). Here the gravitational potential $\phi(r)$ of a homogeneous sphere of radius R_{SF} and total mass M_{dyn} was considered:

$$\phi(r) = \begin{cases} -\frac{3GM_{dyn}}{2R_{SF}} \left(1 - \frac{r^2}{3R_{SF}^2}\right) & \text{if } r \leq R_{SF} \\ -\frac{GM_{dyn}}{r} & \text{if } r > R_{SF} \end{cases}$$

The outflow velocity reaches the local sound speed value right at the surface of the star-forming region, then it accelerates rapidly to reach its terminal value of $\sim 740 \text{ km s}^{-1}$ at a distance about 4 kpc from the galaxy center. At this distance, it already exceeds the escape velocity and thus composes a supergalactic wind. Panels (b) and (c) present the distributions of temperature and density in the flow. The temperature drops from $\sim 2 \times 10^7$ K inside of the star-forming region to $\sim 2 \times 10^6$ K at a 10 kpc distance from the galaxy, whereas the density drops from

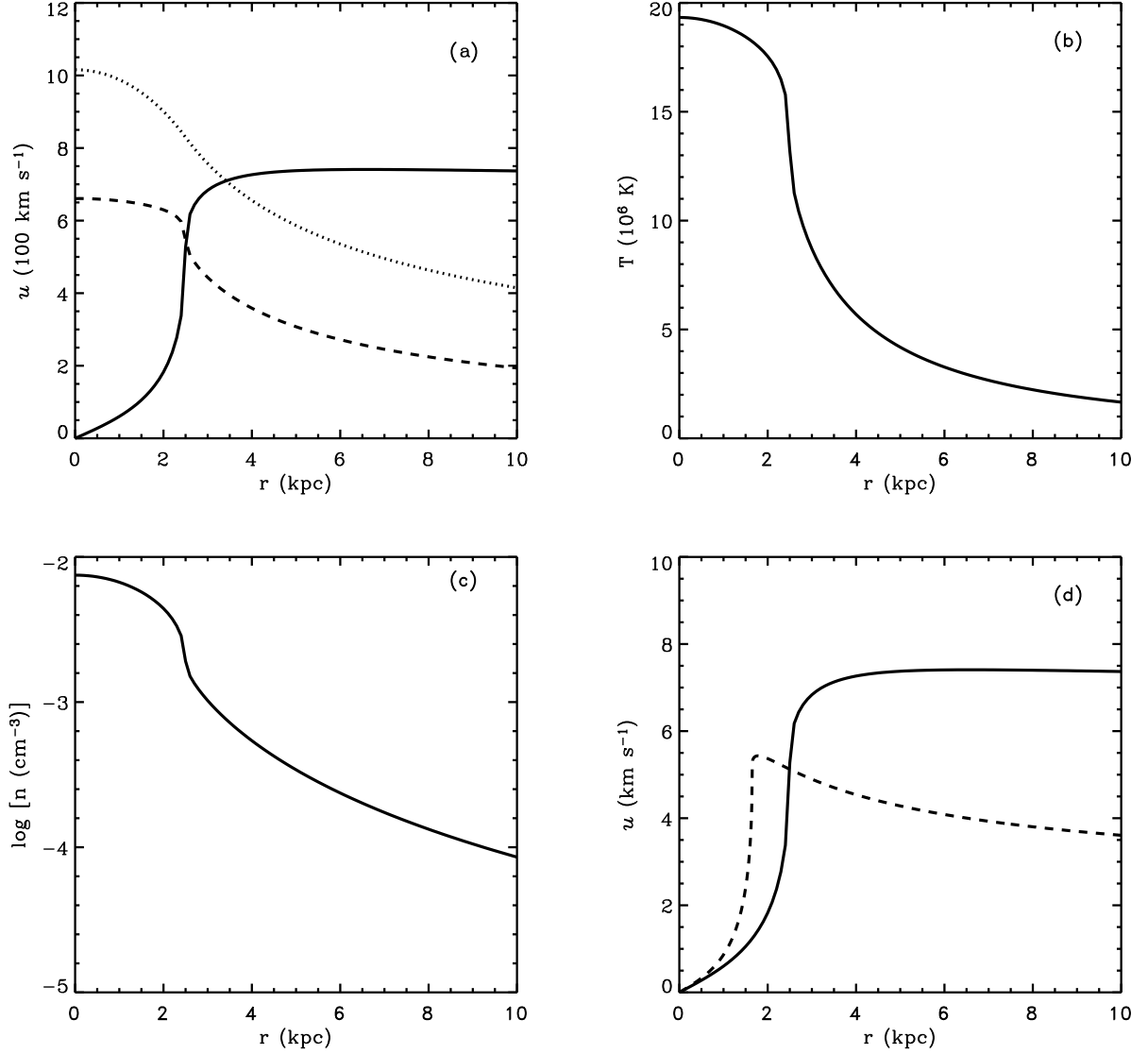


Figure 3.2: Distribution of hydrodynamical variables in the supergalactic wind outflow. The calculations were provided for a proto-galaxy with a dynamical mass of $M_{dyn} = 2 \times 10^{11} M_{\odot}$, $R_{SF} = 2.5$ kpc, $\text{SFR} = 2 M_{\odot} \text{ yr}^{-1}$ and $\eta_d = 0.5$ (model 1). Panels (a), (b) and (c) present the run of velocity, temperature and particle number density, respectively. The dotted and dashed line in panel (a) display the local sound speed and the value of the escape velocity, respectively. Panel (d) compares the velocity distribution in two proto-galactic winds emerging from sources of different size (model 1 and 2, solid and dashed lines, respectively).

$\sim 4 \times 10^{-3} \text{ cm}^{-3}$ to less than 10^{-4} cm^{-3} value. Such protogalactic winds should be detected as sources of a diffuse X-ray emission, as in the case in the local universe (e.g., Chevalier 1992; Strickland & Stevens 2000; Silich et al. 2005; Strickland & Heckman 2009):

$$L_X = 4\pi \int_{R_{st}}^{R_{out}} r^2 n^2 \Lambda_X(T, Z) dr \quad (3.4)$$

where $n(r)$ is the atomic number density, $\Lambda_X(T, Z)$ is the X-ray emissivity (see Strickland & Stevens 2000), and R_{out} marks the distance at which the calculations were stopped, usually set to 10 kpc. We set the lower integral limit to R_{st} assuming that the X-ray emission interior to it is completely absorbed by the accumulated gas. The model predicts a growth in the X-ray luminosity in the range from 0.3 to 8.0 keV as one considers larger SFRs. It is $L_X \approx 4 \times 10^{-4} L_{SF} \approx 2 \times 10^{38} \text{ erg s}^{-1}$ and reaches $L_X \approx 0.1 L_{SF} \approx 3 \times 10^{43} \text{ erg s}^{-1}$ (Compare to Laird et al. 2010) in the case of model 1 with a low SFR and model 4 with a high SFR, respectively. Note that the X-ray emission is concentrated toward the star-forming region, where the density of the X-ray plasma reaches its maximum value and that in protogalaxies with a high SFR a significant fraction of this emission may be absorbed by numerous dense proto-stellar clouds.

However, in the case of SCUBA sources gravity may affect the outflow significantly. Indeed, the escape speed at the surface of scuba

sources, $V_{esc} = (2GM_{dyn}/R_{SF})^{1/2}$, may reach $\sim 1000 \text{ km s}^{-1}$, value which is approximately 10 times larger than in the case of young stellar clusters. In many cases, it is larger than the sound speed in the thermalized plasma, and thus larger than the outflow velocity at the surface of the protogalactic cloud. The larger impact of gravity on the flow for progressively more compact systems with the same mass is shown in Figure 3.2 panel (d), which compares the run of velocity for models 1 and 2 (solid and dashed lines, respectively). The maximum velocity is much smaller, and the flow velocity drops significantly with distance to the protogalactic cloud in the case of more compact star-forming region (model 2, dashed line). Nevertheless, it ends up exceeding the escape velocity value at a larger distance from the protogalaxy center, forming a supergalactic wind.

3.3.2 The bimodal hydrodynamic solution

Protogalaxies which lie above the threshold line (models 4 and 5) radiate a large fraction of the energy input rate within the star-forming volume, which leads to a bimodal hydrodynamic solution (Tenorio-Tagle et al. 2007; Wünsch et al. 2008). In this case, radiative cooling rapidly depletes the thermal energy (and pressure) of the thermalized plasma in the densest central regions of the assembled galaxy, inhibiting the fast acceleration required to reach the sufficient speed to leave the star-

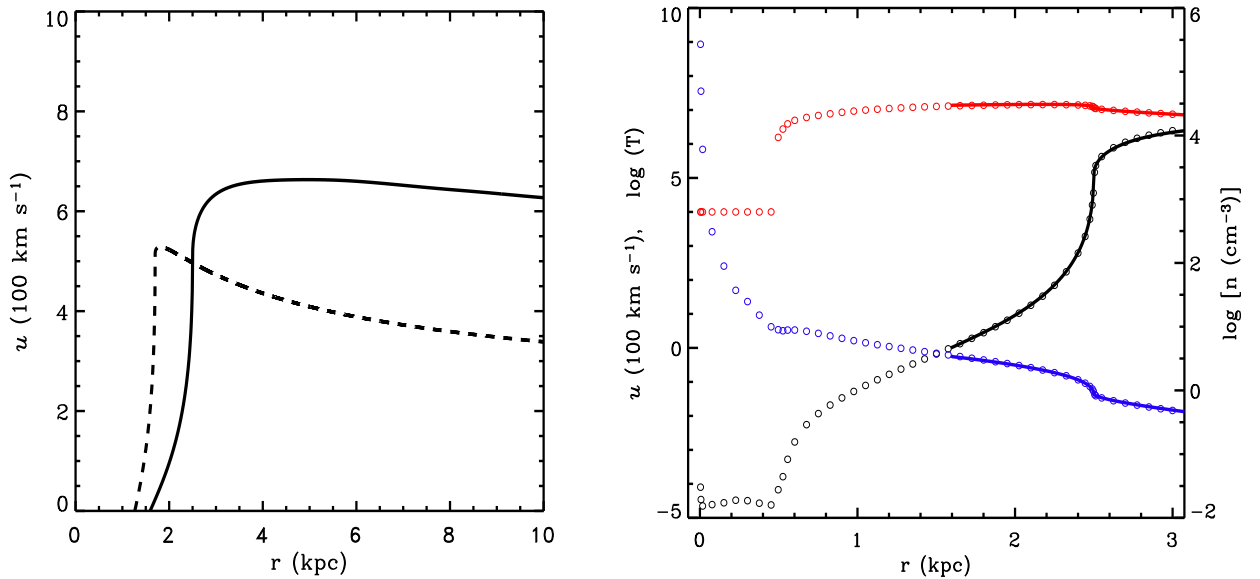


Figure 3.3: Flow velocity profiles for proto-galactic sources evolving in the bimodal hydrodynamic regime. The calculations were carried out for a proto-galactic cloud with a dynamical mass of $M_{dyn} = 2 \times 10^{11} M_{\odot}$, $SFR = 1200 M_{\odot} \text{ yr}^{-1}$ and $\eta_d = 0.5$. The left panel presents the velocity obtained from the semi-analytic calculations for proto-galaxies with $R_{SF} = 2.5 \text{ kpc}$ and $R_{SF} = 1.7 \text{ kpc}$ - solid and dotted lines, respectively. In the right panel, the semi-analytic solution (solid lines) for model 4 is compared with the complete solution from the numerical simulations (open circles) where, the red, blue and black tracks represent the temperature, density and velocity distributions, respectively. Note the excellent agreement between the two methods in the location of the stagnation point and the profiles of the hydrodynamic variables outside the stagnation radius.

forming region. This prompts the stagnation radius, R_{st} , to move out of the starburst center as is shown in Figure 3.3, left panel, where the solid and dotted lines display the semi-analytic results for models 4 and 5, respectively. Inside the stagnation radius, the combination of fast

radiative cooling and gravity prevent the stationary solution and thus full numerical calculations are required in order to have the complete solution (Tenorio-Tagle et al. 2007; Wünsch et al. 2008). The complete hydrodynamic solution in the case of model 4 is shown in Figure 3.3, right panel. Here the results from numerical simulations (open circles) carried out with our Eulerian hydrodynamic code are compared with the semi-analytic hydrodynamic variable distributions: velocity (black line), density (blue line) and temperature (red line). The numerical simulations are in excellent agreement with the semi-analytic results in both, the position of the stagnation point and in the profiles of the hydrodynamic variables in the region $r > R_{st}$. In the bimodal regime density grows and temperature drops smoothly inside the stagnation radius until a thermal instability sets in the flow depleting the temperature to the minimum value allowed in the calculations (10^4 K), see the blue and red profiles. Thus, above the threshold line the matter injected by massive stars and ablated from protostellar clouds inside the stagnation volume remain bound and could be reprocessed into new generation of stars despite the large amount of energy supplied by stellar winds and supernovae explosions. At the same time, the matter deposited by massive stars outside of this volume flows away from the star-forming region as a supersonic wind.

3.3.3 The gravitationally bound solution

The impact of gravity becomes a crucial issue if the radius of the protogalaxy is smaller or equal to the critical value, presented in Figure 3.1 by vertical lines for different values of η_{ld} and M_{dyn} . This occurs when the sound speed at the surface of the protogalactic cloud becomes smaller than one half of the escape velocity, and the nominator in the momentum equation (Equation [2.12] in Chapter 2) goes to zero at the surface of the star-forming region. In this case, the flow velocity cannot reach the sound speed value at the star cluster edge, the stationary solution vanishes, and the protogalaxy does not form a supergalactic wind.

Figure 3.4 shows the hydrodynamic variables in the gravitationally bound regime for the case when the stagnation point is at the center. This case corresponds to model model 3 presented in Table 3.1 and the different lines in panels (a)-(d) correspond to different time-steps in the simulation $t = 31.7$ Myr, 63.5 Myr, and 95.2 Myr (solid, dashed, and dotted lines, respectively). Panel (a) displays velocity profiles of the outflow, in this case velocity grows as a function of radius even outside the cluster volume, but it drops as a function of time. Note that despite an evolution in the quasi-adiabatic regime ($R_{st}=0$) the solution never fulfills the condition for a stationary wind solution, i.e., the flow velocity never reaches the sound speed at the star-forming edge, see panel (b)

which displays the Mach number as a function of the distance from the center. Panel (c) shows that the density of the flow grows as a function of time which causes a small depletion in temperature of the flow as the evolution time goes, see panel (d).

Figure 3.5, panels (a)-(d), presents the results of full numerical simulations for a protogalactic cloud with $R_{SF} < R_{crit}$ (model 6) whose stagnation point is out of the center. Here the quasi-adiabatic wind solution for a protogalaxy with $M_{dyn} = 2 \times 10^{11} M_{\odot}$, $R_{SF} = 2.5$ kpc, $SFR = 40 M_{\odot} \text{ yr}^{-1}$, and $\eta_{ld} = 0.5$ was used as the initial condition for simulations. However, the time evolution was followed assuming the input parameters of model 6 (see Table 3.1). The initial wind solution transforms rapidly into a complex flow with a number of discontinuities and negative velocities inside the star-forming region, see panel (a). Note that the stagnation radius is in this case at ~ 1 kpc. However, the matter deposited between this radius and the edge of the star-forming region is unable to produce a superwind and instead it cools down and ends up falling toward the center. As can be seen in panel (b) which presents the Mach number as a function of radius for positive velocities of the flow, neither the solution in this case reaches the sound speed at the star-forming radius, $R_{SF} = 1.2$ kpc. Our open boundary condition does not allow for the accumulation of this gas and that leads after a readjustment period to a recurrent cycle in which some fraction of the deposited matter first flows away but then cools down and falls

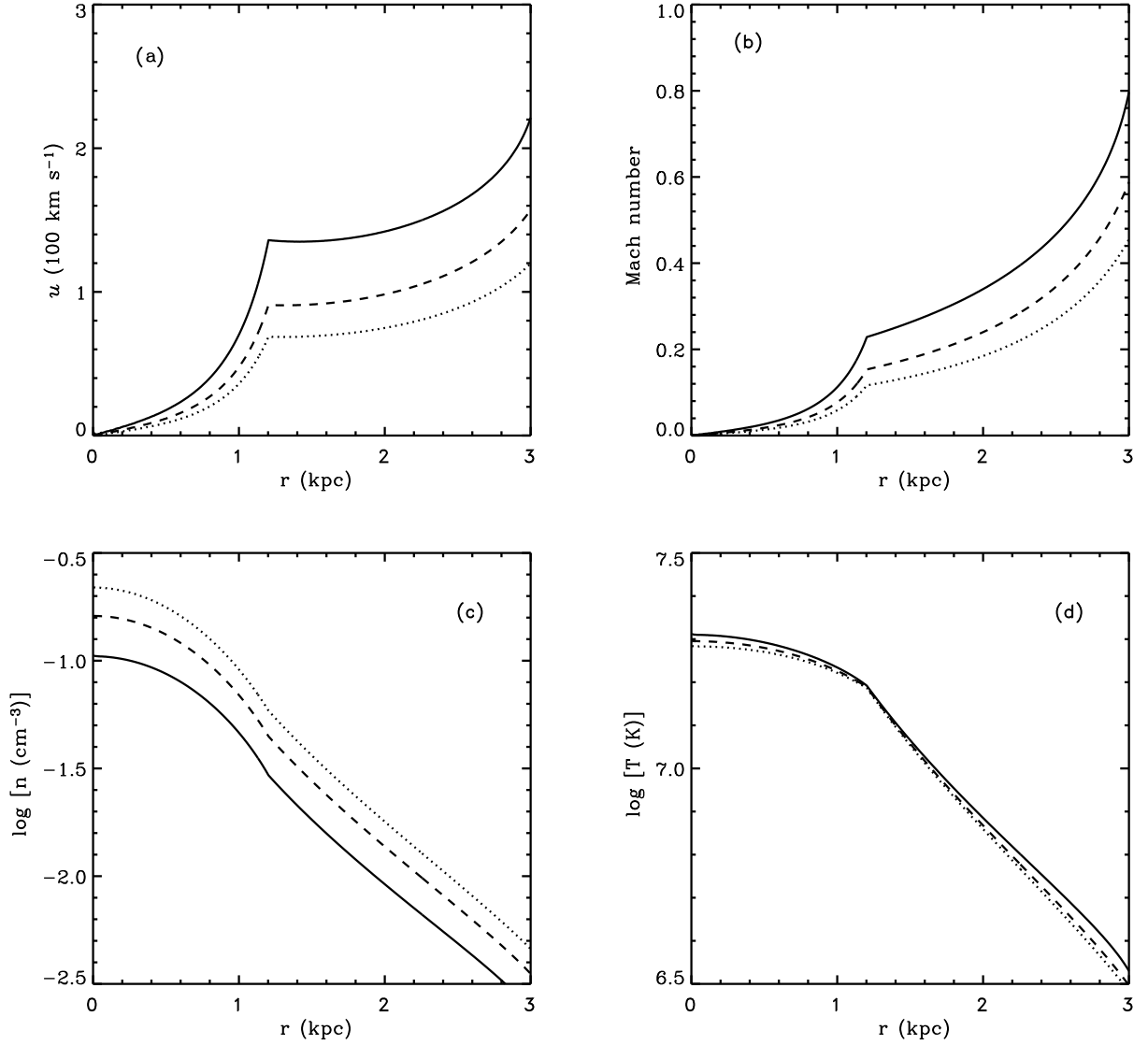


Figure 3.4: Gravitationally bound regime in the case $R_{st} = 0$. Panels (a)-(d) present runs of velocity, Mach number, density and temperature at $t = 31.7 \text{ Myr}$, 63.5 Myr , and 95.2 Myr (solid, dashed and dotted lines, respectively) in the case of model 3. Even a quasi-adiabatic evolution in this case the flow never reaches the stationary wind solution.

back toward of the star-forming region. This causes the compression and storage of the hot gas into a dense shell, which is driven inwards by gravity. The supersonic encounter of the outer gas with the dense shell results into the formation of a shock wave. This at later times ($t > 30$ Myr; dotted lines in Figure 3.5, panels (a),(c) and (d)) produces the parcel of hot gas in-falling behind the cold shell. The shell drives at all times a sound wave into the hot inner zones, which results into noticeable enhancement of temperature and speeds up the in-falling gas ahead of the shell as displayed by the dotted line in Figure 3.5, panels (b)-(d). In this case the simulation ends up at ~ 30 Myr when all matter located inside a computational domain is falling toward the center of the protogalactic cloud. Thus, compact protogalaxies with $R_{SF} < R_{crit}$ trap the injected matter and are not able to form superwinds regardless of their energy output or SFR. A number of semi-analytic calculations have led us to infer that below the mechanical luminosity threshold line, R_{crit} becomes slightly smaller for protogalaxies with a given M_{dyn} , and η_{ld} and a decreasing SFR. However, the calculations showed that the difference in the value of the critical radius usually does not exceed ~ 100 pc. Therefore, we have adopted the value of R_{crit} , calculated for a protogalaxy with the threshold SFR as the gravitationally bound limit for all galaxies with the same M_{dyn} and η_{ld} . The adopted critical radii, R_{crit} , for galaxies with various M_{dyn} and η_{ld} are displayed in Figure 3.1 by thin vertical lines. Figure 3.6 shows the critical radius as a

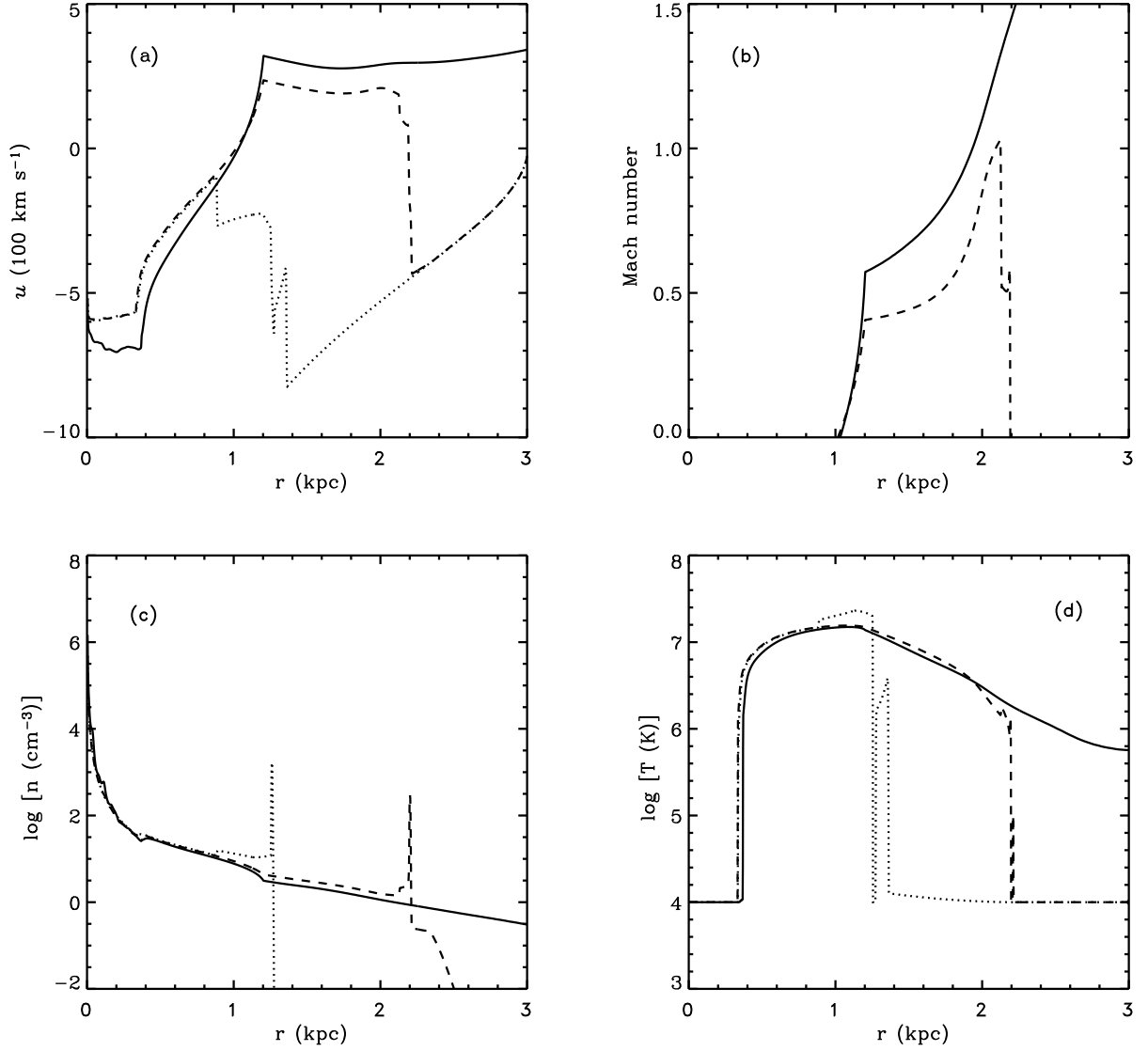


Figure 3.5: Gravitationally bound regime in the case $R_{st} > 0$. Panels (a)-(d) present runs of velocity, Mach number, density and temperature at $t = 22.2 \text{ Myr}$, 29.5 Myr and 31.4 Myr (solid, dashed and dotted lines, respectively) of model 6. Note that panel (b) presents the Mach number only for positive velocities of the flow. Note also that in this case the flow is bimodal, $R_{st} > 0$, however, the pressure gradient between the stagnation radius and the starburst edge is unable to produce a superwind and eventually all mass deposited in this region falls toward the center.

function of the ablation coefficient η_{ld} for protogalaxies with dynamical masses $M_{dyn} = 8 \times 10^{11} M_{\odot}$ and $M_{dyn} = 2 \times 10^{11} M_{\odot}$, presented by the dashed and solid lines respectively. If one fixes η_{ld} , M_{dyn} and SFR, and one considers more and more compact star-forming regions the system reaches its critical radius, then protogalaxies whose $R_{SF} < R_{crit}$ are in the gravitationally bound regime. Note also that for fixed parameters of the star-forming region (dynamical mass, size and SFR) the system could become gravitationally bound if the ablation coefficient takes larger values.

Note that in very high redshift systems (i.e., just forming galaxies) the metallicity would be extremely low and hence radiative cooling will be substantially lowered. This could potentially have a large effect on the dynamics of the reinserted matter, favoring outflows. While this may be true for the first galaxies, observationally it is known that the metallicity of high redshift systems can be large in some cases, reaching values of several times solar. If metallicity grows rapidly as the galaxy forms, then radiative cooling will be even stronger than that predicted in our calculations further favoring the retention of the reinserted material. The threshold SFR line in Figure 3.1 moves up a factor of 1.5 approximately in the case of the first galaxies with a metallicity $Z = 0.1 Z_{\odot}$ and approximately 4.5 times down for older systems with a super solar abundance ($Z = 10 Z_{\odot}$). However, the critical radii, R_{crit} , remains almost identical as one considers different metallicities.

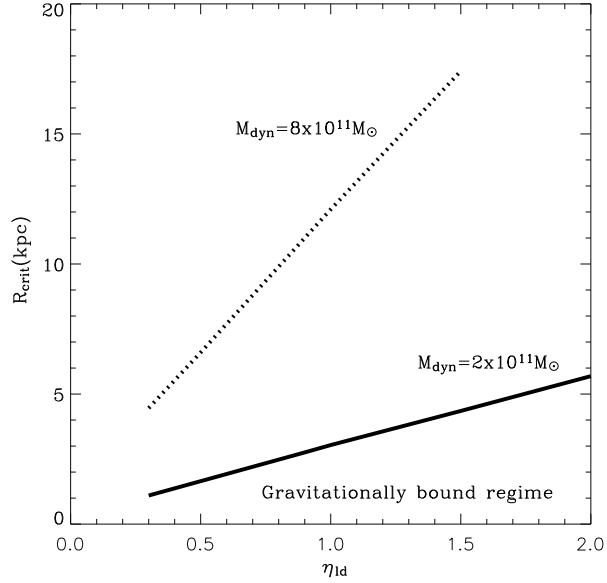


Figure 3.6: Critical size (R_{crit}) of star-forming regions as a function of the ablation parameter η_{id} and the dynamical mass of the proto-galaxy. The superwind feedback mode is inhibited in proto-galaxies with $R_{SF} < R_{crit}$. The matter returned by massive stars and ablated from star-forming regions remains buried inside the star forming volume and as it accumulates it should lead to further stellar generations. The calculations were provided for proto-galactic clouds with $0.3 \leq \eta_{id} \leq 2$ and dynamical masses of $M_{dyn} = 2 \times 10^{11} M_{\odot}$ (solid) and $M_{dyn} = 8 \times 10^{11} M_{\odot}$ (dotted) lines, respectively.

3.4 Discussion

The thermalization of the kinetic energy provided by vigorous star formation in young forming galaxies may lead to three different hydrodynamic regimes, depending on the rate of star formation, the protogalaxy total mass and radius, and the rate of mass loading from protostellar

clouds. Note that the value of the ablation parameter η_{ld} remains free in the theory. However, one can get an idea about which values of η_{ld} are reasonable considering sources without a secondary star formation, which evolve in the superwind regime. Then one can notice that in the case of star formation with a constant SFR, which terminates when the initial gas reservoir is completely exhausted, the global star formation efficiency, ϵ_* , defined as the ratio of the stellar mass, M_* , to the initial mass, M_{PG} , of the protogalactic cloud at this moment will be

$$\epsilon_* = \left(SFR - \frac{2L_0}{V_{A,\infty}^2} \frac{SFR}{1 \text{ M}_\odot \text{ yr}^{-1}} \right) (SFR + \eta_{ld} SFR)^{-1} = \frac{0.9}{1 + \eta_{ld}}. \quad (3.5)$$

In Equation [3.5], the stellar mass, M_* , was calculated as the difference between the mass of stars formed during the evolutionary time t and that reinserted by supernovae explosions and stellar winds:

$$M_* = (SFR - \dot{M}_{SF}) \times t = \left(SFR - \frac{2L_0}{V_{A,\infty}^2} \frac{SFR}{1 \text{ M}_\odot \text{ yr}^{-1}} \right) \times t, \quad (3.6)$$

and the initial mass of the system, M_{PG} , is

$$M_{PG} = (1 + \eta_{ld}) \times SFR \times t \quad (3.7)$$

The star formation efficiency would then be $\epsilon_* = 90\%$ if $\eta_{ld} = 0$ and approaches $\approx 30\%$ value required to form a gravitationally bound system (e.g., Geyer & Burkert 2001) when $\eta_{ld} = 2$. Note that the required

star formation efficiency may be smaller, and thus the upper limit for η_d larger, if one considers a slow expulsion of the injected gas from the system (Baumgardt & Kroupa 2007). The predictions are thus that massive star-forming protogalaxies with large SFRs similar to those detected in SCUBA sources ($\geq 10^3 M_\odot \text{yr}^{-1}$) evolve in a positive star formation feedback conditions: either in the bimodal, or in the gravitationally bound regime. Only protogalaxies evolving in the bimodal regime will form supergalactic winds as is in the case of submillimeter galaxies SMM J14011+0252 (Nesvadba et al. 2007) and, probably, SMM J221726+0013 (Bower et al. 2004). Inevitably then, matter accumulation would follow in the central zones or in the whole protogalactic volume. Radiative cooling would then reduce the injected gas temperature, which would promote an even stronger cooling and recombination, making the accumulated gas an easy target of the UV radiation field. Photoionization of this gas is to set an equilibrium temperature ($T_{HII} \leq 10^4$ K), but its accumulation will drive it Jeans unstable, leading unavoidably to its collapse and to the formation of new stars. Many stellar generations are expected in this scenario, until most of the mass, through its continuous recycling, has been converted into low mass stars with $M \leq 7 M_\odot$. The resultant stellar populations and the ISM would then show a large metallicity spread. Consequently, if the formation of large stellar spheroids (galaxy bulges or elliptical galaxies) occurs through a process of rapid matter accumulation and further

conversion of this matter into stars (e.g., Swinbank et al. 2006), which would imply a large SFR, the expectations are thus that little or none of the returned matter, through winds and SN explosions, is going to be ejected out of the system. Instead it is to be reprocessed into further episodes of stellar formation. This implies that the largest episodes of star formation would leave little trace of their stellar evolution into the intergalactic medium leading instead to a fast metal enrichment of the interstellar gas, as observed in high redshift quasars (e.g., Hamann & Ferland 1999; Juárez et al. 2009).

3.5 Conclusions

This chapter shows that the thermalization of the kinetic energy provided by vigorous star formation in young forming galaxies may lead to three different hydrodynamic regimes, depending on the rate of star formation, the protogalaxy total mass and radius, and the rate of mass loading from protostellar clouds. Large galaxies with low SFRs and small ablation coefficient η_{ld} form supersonic winds which carry from the star formation regions the matter returned by massive stars and that ablated from protostellar clouds. Similar galaxies located in the SFR- R_{SF} parameter space above the threshold line lose via a superwind a fraction of the deposited matter. The matter deposited by massive stars and that ablated from star-forming regions in the inner

zones of such galaxies becomes thermally unstable due to strong radiative cooling, accumulates and is to be re-processed there into secondary star formation. Finally, the thermal pressure in compact sources with radii $R_{SF} \leq R_{crit}$ is unable to withstand the gravitational pull of the galaxy. In such cases, protogalaxies retain all the reinserted and ablated matter within the protogalaxy volume and do not form supergalactic winds. The hydrodynamics of nuclear star-bursting galaxies with a central supermassive black hole is the subject of the second part of the dissertation and is presented in the next chapter.

Chapter 4

The hydrodynamic interplay between SMBHs and nuclear starbursts

4.1 Introduction: the nuclear starburst-SMBH interplay

This chapter presents a comprehensive study of the hydrodynamics of spherically symmetric flows driven by young, massive nuclear starbursts (NSBs) with a central supermassive black hole (SMBH) and shows that the solution depends on the location of the system in the parameter space defined by L_{NSB} - R_{NSB} - M_{SMBH} ¹. The three possible hydrodynamic regimes in this case are similar to those studied in Chapter 2, however, in this case all possible solutions are bimodal. They present

¹Here L_{NSB} and R_{NSB} are the mechanical luminosity and radius of the nuclear starburst, and M_{SMBH} the mass of the supermassive black hole.

a starburst wind flow driven by the high thermal pressure that results from the thermalization of the injected matter inside the starbursts volume and an accretion flow defined by the matter that remains locked in the central region because of the gravity pull and strong radiative losses. The amount of matter that forms the accretion flow and the wind depends only on the stagnation radius, R_{st} , the radius at which the flow velocity is zero. Thus the value of the stagnation radius defines both the upper limit for the accretion rate onto the central black hole, as we do not consider rotation, and the amount of matter that leaves the nuclear cluster in the form of a wind. Figure 4.1 shows the three possible hydrodynamic regimes. The critical luminosity marked by solid line separates the quasi-adiabatic regime for low mass NSBs ($L_{NSB} \leq L_{crit}$) with small accretion rates onto the central SMBH from the catastrophic cooling regime ($L_{NSB} > L_{crit}$) with high accretion rates. The region to the left of the critical radius, marked by the dashed line, represents the gravitationally bound regime where all the returned mass eventually remains locked inside the starbursts volume and falls toward the center, this solution may drives also a positive feedback condition within the starburst volume.

In this chapter we use the hydrodynamical model for a star-bursting region with a central black hole presented in Chapter 2. In this case the mechanical luminosity $L_{NSB} = \dot{M}_{NSB}/V_{A,\infty}^2$ has been normalized to the average mechanical luminosity for an instantaneous starburst with

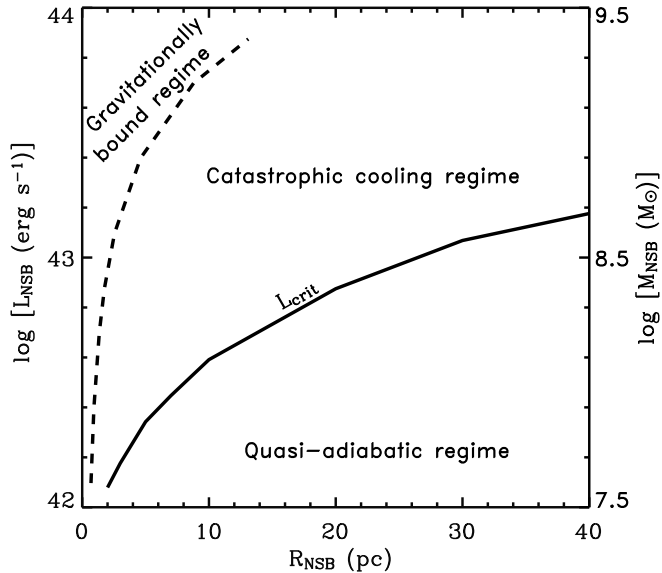


Figure 4.1: The three possible hydrodynamic regimes for the bimodal flows. The solid line represents the critical energy (L_{crit}) which separates the quasi-adiabatic regime with subsonic accretion flows and small accretion rates from the catastrophic cooling regime with supersonic inflows and high accretion rates. The dashed line displays the critical radius which separates the gravitationally bound regime from the other two regimes. This solution results into a positive feedback condition where all the injected matter falls toward the center.

a Salpeter initial mass function, sources between $1 M_{\odot}$ and $100 M_{\odot}$ and with ages less than 10 Myr, $L_{NSB} = 3 \times 10^{40} (M_{NSB}/10^6 M_{\odot}) \text{ erg s}^{-1}$ (Leitherer et al. 1999). It is assumed $V_{A,\infty} = 1500 \text{ km s}^{-1}$ and solar metallicity in all calculations, unless it is explicitly mentioned. Section 4.2 presents the hydrodynamics of the bimodal flows produced in the quasi-adiabatic regime, in this case we used the semi-analytic model

presented in Chapter 2, section 2.3. The case of very massive starbursts with a central SMBH evolving in the strong radiative cooling regime is presented in section 4.3, in this case we used full numerical simulations in order to find the complete hydrodynamic solution, see section 2.4 in Chapter 2. The gravitationally bound regime is presented in section 4.4, in this case the solution is not stationary and thus full numerical simulations are required. Section 4.5 presents the upper limits for the SMBH accretion rate and luminosity for various cases, models in the quasi-adiabatic and catastrophic cooling regimes. This section presents also a discussion on the possible impact of the resultant nuclear starburst winds on the interstellar medium. The predicted contribution of the accretion flows to the X-ray emission is presented in section 4.6. The conclusions of this chapter is given in section 4.7. The main results of this chapter are published in Silich et al. (2008) —the semi-analytic model and Hueyotl-Zahuantitla et al. (2010) —1D numerical simulations.

4.2 Bimodal solution in the quasi-adiabatic regime

This section presents the bimodal hydrodynamic solution of the matter reinserted by relatively low mass nuclear starbursts which host a central SMBH. In the case of low mass clusters (below the threshold energy, L_{crit} , presented in Figure 4.1) radiative losses are not so important and

the complete solution can be obtained with the semi-analytic approach presented in Chapter 2. Thus in order to find the bimodal solution (the accretion and wind solution) one needs two boundary conditions in addition to the parameters of the system. The next section describes the method to select the proper solution from a family of integral curves. The results of this section are published in Silich et al. (2008)

4.2.1 Boundary conditions and the appropriate solution

The thermalization of the mechanical energy supplied by the massive stars within a young stellar cluster causes a large thermal overpressure that drives away the injected matter in the form of a high-velocity outflow —the star cluster wind (Chevalier & Clegg 1985; Cantó et al. 2000; Silich et al. 2004). The smooth transition from a subsonic expansion of the high-temperature thermalized ejecta, inside the nuclear starburst volume, to the supersonic free wind outflow at $r > R_{NSB}$ requires the sonic point (the point where the outflow velocity is equal to the local sound speed) to be located at the star cluster edge (Cantó et al. 2000; Silich et al. 2004), see equations [2.9] and [2.12] in Chapter 2. Hereafter we will refer to this sonic point as the *outer* sonic point, $R_{s,o}$. In the case of nuclear star clusters with a central supermassive black hole, the gravitational pull from the SMBH prevents the escape of the injected matter from the central zones of the cluster and thus shifts the stagnation point, the point where the flow velocity is zero,

from the star cluster center to a larger radius. In this case all mass continuously deposited by the cluster inside the central zone, limited by the stagnation radius, R_{st} , cannot escape from the gravitational well of the central SMBH and composes the accretion flow. The presence of the SMBH results in a second sonic point, between the stagnation point and the center of the stellar cluster. To distinguish this sonic point from that at the star cluster surface we will refer to it as the *inner* sonic point, $R_{s,i}$.

Thus, the stagnation radius defines the upper limit to the accretion rate onto the central SMBH and also the fraction of mass that the cluster returns to the ambient ISM. From pure geometrical arguments, the mass that is able to fuel the central SMBH is some fraction of the total mass deposited by the nuclear starburst:

$$\dot{M}_{acc} = \dot{M}_{NSB} \frac{R_{st}^3}{R_{NSB}^3}. \quad (4.1)$$

This implies that the major problem that one has to solve in order to build the hydrodynamic solution for the bimodal flows that results from the energy and mass deposition by a nuclear starburst with a central SMBH in the quasi-adiabatic regime is reduced to the calculation of the stagnation radius.

In the semi-analytic model, the proper position of the stagnation point is defined by the second boundary condition, the *inner* sonic point, which is similar to that in the case of a Bondi accretion flow

with $\gamma = 5/3$, Bondi (1952). Specifically, the *inner* sonic point must be located at the center of the cluster. However, in the case of very massive and compact nuclear starbursts, when radiative cooling becomes an important factor, the accretion flow becomes supersonic at some distance out of the center, see section 4.3. To avoid numerical problems associated with the central singularity, here the proper solution is selected according with two boundary conditions: the *inner* sonic point must lie at the last stable orbit associated with the central black hole

$$R_{s,i} = 3R_{Sh}, \quad (4.2)$$

where R_{Sh} is the Schwarzschild radius of the central black hole, and the *outer* sonic point must be located at the star cluster border, $R_{s,o} = R_{NSB}$. In order to find the proper integral curve we take a trial stagnation radius and then select the temperature, T_{st} , from the outer boundary condition (Silich et al. 2004; Tenorio-Tagle et al. 2007). Then the gas number density is calculated according to equation [13] and finally, the values of R_{st} , T_{st} , and n_{st} are used as initial condition to the backward integration from R_{st} toward the starburst center.

Figure 4.2, left panel, presents the results of the integration of equations [2.7]-[2.12] (inside and outside the cluster volume) for different values of the trial stagnation radius. If the selected R_{st} is too large, the backward integration of equations [2.7]-[2.9] leads to a double-valued, unphysical solution (dashed line). In this case the turn off point,

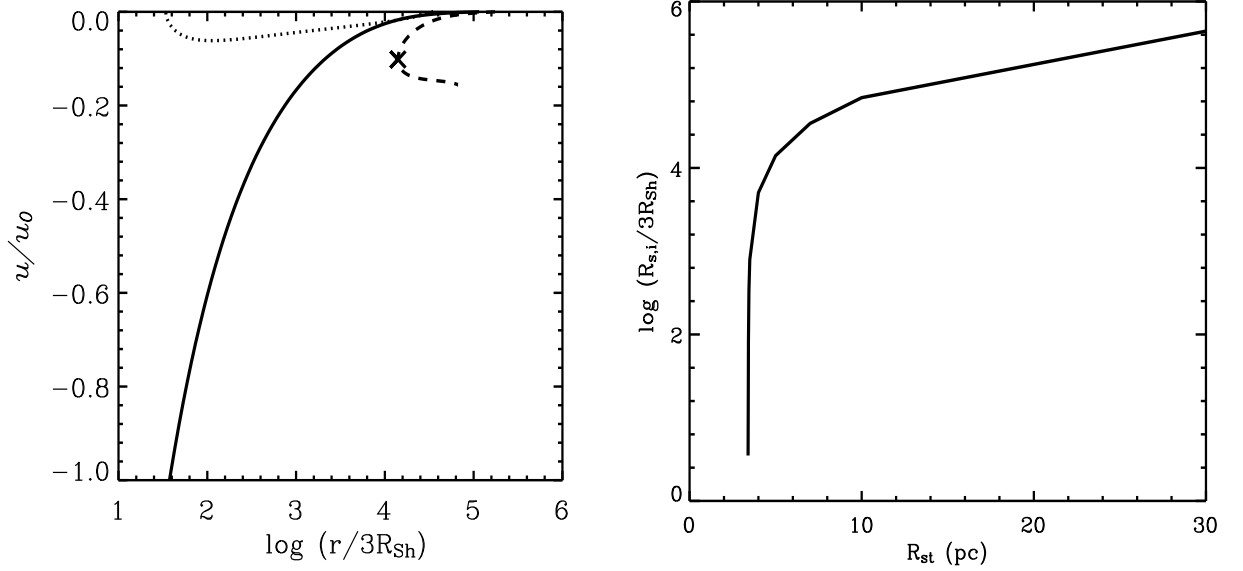


Figure 4.2: Structure of the integral curves for different stagnation radii. The integral curves in the *left panel* marked by dashed, solid and dotted lines correspond to stagnation radius: 5 pc, 3.3 pc, and 1 pc, respectively. The dashed line represents the transonic unphysical solution, in this case the sonic point coincides with the turn of the line, and is marked by a cross. The solid line shows the selected solution that satisfies both boundary conditions. The dotted line presents another unphysical branch of integral curves that tends toward positive flow velocities around the black hole. The normalization velocity are $u_0 = 10^4 \text{ km s}^{-1}$ for solid and dashed lines, and $u_0 = 10^2 \text{ km s}^{-1}$ for the dotted line. The *right panel* shows the position of the inner sonic point as function of the considered stagnation radius. These calculations assumed a starburst of mass $M_{NSB} = 10^8 M_\odot$, radius, 100 pc, and a black hole mass $M_{SMBH} = 10^8 M_\odot$. In this particular case $R_{st} = 3.3 \text{ pc}$.

marked by a cross, in the velocity profile coincides with the sonic point far from the cluster center. The turn off point moves toward the center when the considered R_{st} is smaller, and finally this leads to the proper integral curve (solid line) that approaches the last stable orbit with the

sound speed, see the right panel in Figure 4.2. For even smaller values of R_{st} the solution is always subsonic, however it never fulfills the *inner* boundary condition and instead the velocity goes to zero as it is shown in left panel by the dotted line. Although the inner boundary condition here used (presented by equation [4.2]) is in some respect arbitrary, Figure 4.3 demonstrates that the location of the stagnation radius is a weak function of the assumed value of $R_{s,i}$ and thus the *inner* boundary condition does not affect the solution significantly. However, here the proper solution is selected such that the backward integration fulfills the condition [4.2].

Figure 4.4 present the distribuion of the flow variables (velocity, number density and tempretaure) for a particular case: a $10^8 M_\odot$ black hole located at the center of a nuclear starburst with mass $M_{NSB} = 10^8 M_\odot$ and radius $R_{NSB} = 40$ pc. In this case the stagnation radius, marked by the dotted line in panel (a), is $R_{st} = 2.7$ pc. At larger radii the velocity grows almost linearly to reach the sound velocity at the star cluster surface and then becomes supersonic outside the cluster surface, and approaches soon its terminal value, some what smaller than the adiabatic wind terminal speed as radiative losses deplete some energy inside the starburst and in the free wind region. In the region between the stagnation radius and the black hole, the matter deposited by stellar winds and supernovae composes a stationary accretion flow. The absolute value of velocity grows rapidly in this region. However

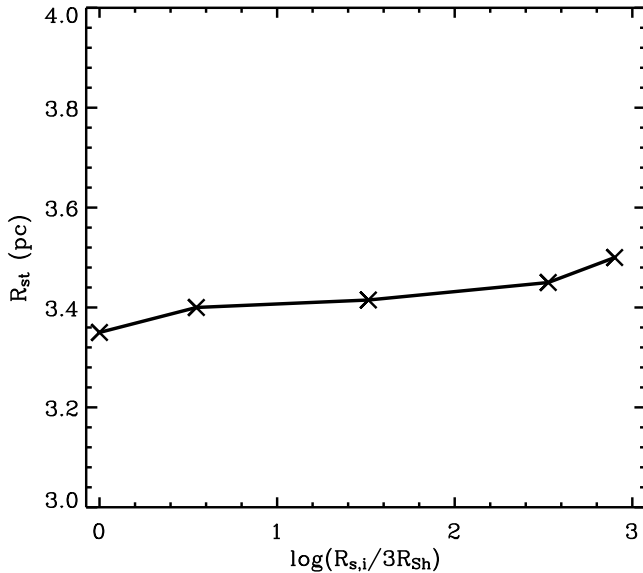


Figure 4.3: Impact of the inner boundary condition on the value of the stagnation radius. the calculations were provided for five different values of inner sonic radius: $R_{s,i} = 3R_{Sh}$, $10.5R_{Sh}$, $98R_{Sh}$, $1009R_{sh}$, and $2385 R_{Sh}$. The starbursts and black hole parameters are identical to those in Figure 4.2.

the accretion flow remains subsonic (see panel (d) that shows the Mach number against radius for this case) as radiative losses are not able to compensate for the heating of the in-falling matter. Despite the rapid increase in density (panel (a)) and thus of cooling, temperature grows rapidly (see panel (c)) due to the fast compression of the in-falling matter onto the central SMBH. Note that in this case the accretion flow remains subsonic even at $\sim 2 \times 10^{-4}$ times the last stable orbit for the considered black hole. The hydrodynamic solution in the case of

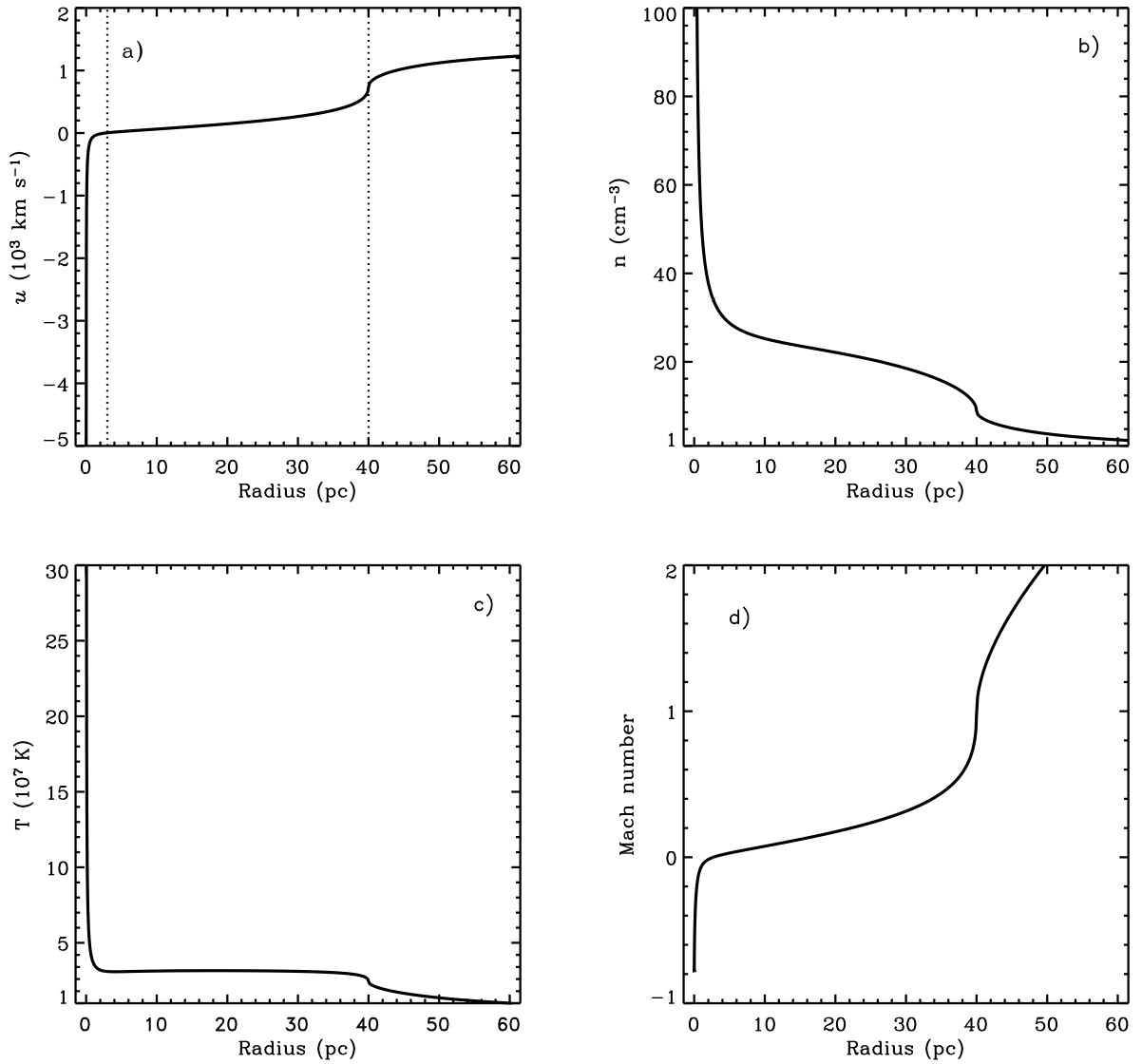


Figure 4.4: Structure of the flow in the case of a nuclear starbursts with a central supermassive black hole. Panels (a), (b), and (c) show the velocity, number density, and temperature profiles, respectively. Vertical dotted lines in panel (a) mark $R_{st} = 3.3$ pc and $R_{NSB} = 40$ pc, other parameters are given in the text. Panel (d) shows the *outer* sonic point at the cluster edge while the accretion flow remains subsonic, in this case even at a radius $r = 9.5 \times 10^{-9}$ pc.

strong radiative cooling where the accretion flow becomes supersonic and experiments thermal instabilities is the subject of the next section.

4.3 The bimodal solution in the catastrophic cooling regime

The impact of radiative cooling on the inner structure of the flow becomes more and more important for starbursts with larger mechanical luminosities (which is proportional to the star cluster mass). In this section by means of one-dimensional numerical simulations with the hydro-code ZEUS (Stone & Norman 1992), the effect of strong radiative cooling and gravity on the hydrodynamics of the matter reinserted by massive stars within nuclear starbursts with a central SMBH is studied. The main results of this section are published in Hueyotl-Zahuantitla et al. (2010).

The semi-analytic method described in previous section claims that the proper solution (Figure 4.2, solid line) is always in between two families of integral curves: the “c-type” transonic solution and the “u-type” subsonic solution, marked by a dashed and a dotted line in Figure 4.2, respectively. In practice we iterate between these two types of integral curves in order to find the proper solution in the case of models approaching to the critical energy presented in Figure 4.1. However, as we consider more and more massive clusters radiative cooling becomes an

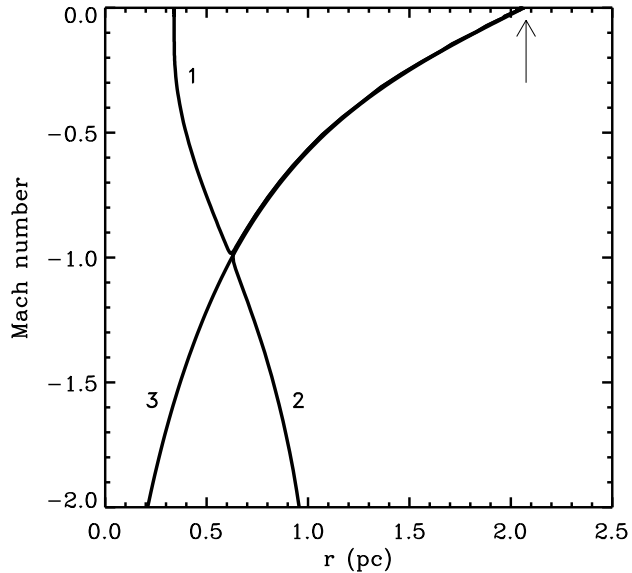


Figure 4.5: Supersonic accretion flow. Mach number as a function of radius for u- and c-type solution marked by labels 1 and 2, respectively. In the case of strong radiative cooling the proper solution requires to pass a special point, the point where both the nominator and the denominator in equation [2.9] used in the semi-analytic approach goes to zero. The complete solution marked by label 3 was found by performing full numerical simulations. The arrow indicates the position of the stagnation point. The parameters of the cluster and black hole are given in the text.

important agent in the central region of the NSB and thus the accretion flow becomes supersonic. The transition from subsonic to supersonic inflow velocities occurs at a special point, when both the nominator and denominator of equation [2.9] goes to zero. Figure 4.5 presents the u- and c-type solutions inside the stagnation radius in terms of the Mach

number (curves marked by labels 1 and 2, respectively) for an extremely compact and massive starburst ($R_{NSB} = 3 \text{ pc}$, $M_{NSB} = 10^8 M_{\odot}$) with a central SMBH, $M_{SMBH} = 10^8 M_{\odot}$. It shows that both solutions have identical initial parameters at R_{st} (marked by the arrow) for the backward integration, nevertheless the solution splits at the special point, R_{sp} , where the proper solution marked by label 3 becomes supersonic. We can not pass through the special point with the current version of our semi-analytic code and thus we use numerical simulations in order to find the accretion flow solution. Here after we use 1D numerical simulations in order to find the complete hydrodynamic solution for the bimodal flows. Note however that the semi-analytic approach can be used to calculate the stagnation radius even in the case of strong radiative cooling.

4.3.1 Initial conditions for the simulations

Here in order to perform the numerical simulations the initial distributions of velocity, pressure, temperature and density were taken from the semi-analytic wind solution (Silich et al. 2008), without accounting for the gravitational pull from the starburst and without SMBH. The method described in Chapter 2, section 2.4, is used to account for the energy and mass deposition inside the NSB, and the gravitational pull of the system. The initial condition is adapted to starbursts of the required size (see Table 4.1).

Table 4.1: The input models

Model	R_{NSB}	M_{NSB}	$\log(L_{NSB})$	L_{NSB}/L_{crit}	\dot{M}_{NSB}
	(pc)	($10^8 M_\odot$)			($M_\odot \text{ yr}^{-1}$)
(1)	(2)	(3)	(4)	(5)	(6)
1a	40	2.0	42.778	0.5	8.45
1b	40	4.0	43.079	1.0	16.89
1c	40	6.0	43.255	1.5	25.34
1d	40	6.8	43.302	1.7	28.72
1e	40	8.0	43.380	2.0	33.79
2a	10	0.3	41.954	0.27	1.27
2b	10	0.5	42.176	0.45	2.11
2c	10	1.0	42.477	0.9	4.22
2d	10	1.67	42.698	1.5	7.03
2e	10	2.22	42.823	2.0	9.38
2f	10	2.75	42.916	2.5	11.61
2g	10	10.0	43.477	9.0	42.23
2h	10	20.0	43.778	18.0	84.46

The starburst input parameters for the simulations. Column 1 is a reference to the models. The radius (R_{NSB}), mass (M_{NSB}), logarithm of mechanical power (L_{NSB} , measured in erg s^{-1}), the ratio of the starburst mechanical power to the critical mechanical luminosity (L_{NSB}/L_{crit}) and the total starburst mass deposition rate (\dot{M}_{NSB}) are presented in columns 2 to 6, respectively. All starburst models have a central SMBH with a mass $M_{BH} = 10^8 M_\odot$.

The reference models are presented in Table 4.1. Here column 1 is a reference to the model, columns 2, 3 and 4 present the radius, mass and mechanical luminosity of the considered starburst, respectively. The ratio of the starburst mechanical luminosity to the critical luminosity and the total mass deposition rate inside the starburst volume are shown in columns 5 and 6. The mass of the central SMBH, unless explicitly mentioned, was assumed to be $M_{BH} = 10^8 M_{\odot}$ in all calculations. The computational domain for models 1a - 1e extends radially from $R_{in} = 0.1$ pc to $R_{out} = 50$ pc. The inner and outer radii of the computational domain in the case of models 2a - 2h are 0.05 and 20 pc, respectively, 1000 grid zones were used in all calculations. The resolution convergency was tested in the case of the most energetic model (2h), carried out with 1000 and 3000 grid cells resolution. The results with both resolutions are in excellent agreement over the whole computational domain. See Appendix B for an analysis of the impact of the inner grid cell-size on the hydrodynamic solution.

4.3.2 Tests of the numerical simulations

In order to test our numerical code, several simulations were carried out for starbursts in the quasi-adiabatic regime to compare them with the semi-analytic model (Silich et al. 2008) presented in previous section. Figure 4.6 presents, as an example, the results of the semi-analytic (solid line) and numerical (open circles) calculations for case 2c in Ta-

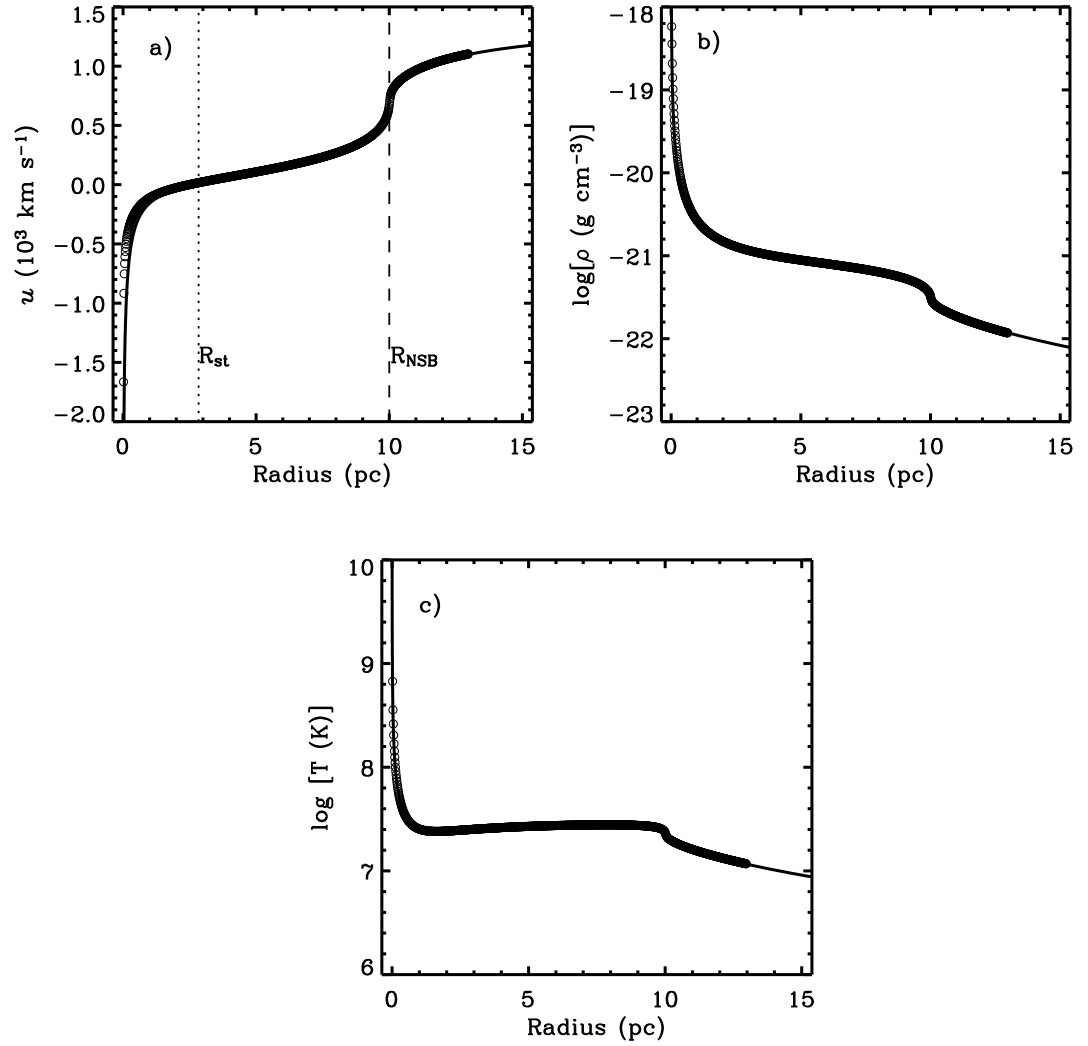


Figure 4.6: Test calculations. The numerical hydrodynamic solution (circles) for model 2c (see Table 4.2) is compared with the semi-analytic results (solid lines). Panels (a)-(c) show the run of the stationary velocity, density and temperature across the radial direction. In panel (a), the dotted and dashed vertical lines mark the location of the stagnation radius and the nuclear starbursts radius, respectively.

ble 4.1. There is a good agreement between the two methods, as shown in panels (a)-(c), for the stationary run of velocity, density and temperature, respectively. The value of the stagnation radius, marked by the dotted line in panel (a), is $R_{st} = 2.8$ pc, only about $\sim 1.5\%$ less than the value predicted by the semi-analytic model. The stationary solution shows how the matter deposited by massive stars inside the stagnation volume ends up falling towards the center and fuels the SMBH. On the other hand, matter reinserted between the stagnation radius and the starburst edge is steadily accelerated to reach its sound velocity at the starburst edge and then it expands supersonically forming the starburst wind. Note that as matter falls to the center its density grows orders of magnitude due to convergency alone (panel (b)). The temperature increases also very sharply (panel (c)) due to the violent compression induced by the rapidly in-falling matter. Note that Figure 4.5 represents an additional test to our numerical code.

4.3.3 The numerical solution above the threshold energy

The hydrodynamic solution for the matter reinserted by massive stars within an evolving young massive starburst in presence of a central SMBH is always bimodal, whether one considers low mass starbursts which evolve in the quasi-adiabatic regime or in very massive starbursts evolving in the catastrophic cooling regime. The main difference is that in massive starbursts strong radiative cooling becomes the physical

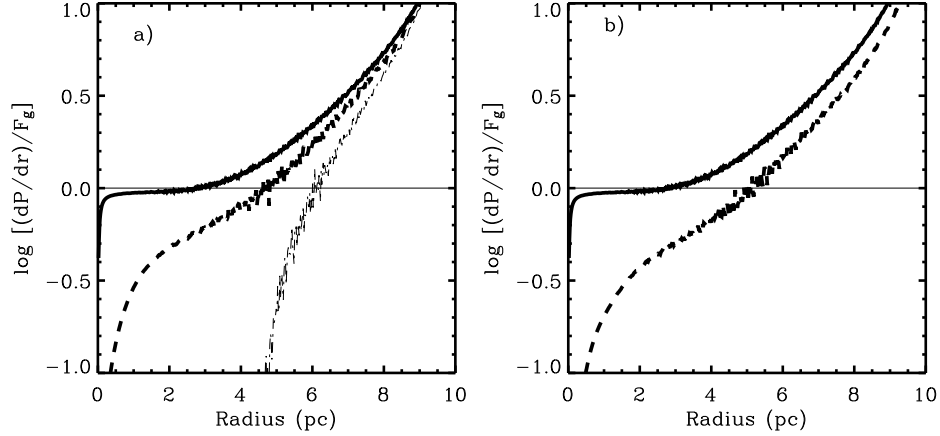


Figure 4.7: The comparison of the pressure gradient to the gravity force inside the starburst volume. Panel (a) shows the ratio of the pressure gradient to the gravity force for starbursts of the same mass and radius (model 2c) but with different gas metallicities. Here solid, dashed and dotted lines correspond to $Z = Z_{\odot}$, $Z = 5Z_{\odot}$ and $Z = 10Z_{\odot}$, respectively. The intersection of the curves with the thin horizontal lines marks the position of the stagnation radius. The stagnation radius moves to a larger distance from the center as the cooling rate becomes larger. Panel (b) shows the same ratio for starburst with different energy deposition rates (or different masses) but the same (solar) metallicity, the solid and dashed lines correspond to models 2c and 2e in Table 4.1, respectively, implying a large R_{st} for a more massive cluster.

agent that defines where the stagnation radius lies. The stationary location of the stagnation radius is well defined by the balance between the gravitational force (F_g) and the outward thermal pressure gradient (dP/dr), which naturally, is strongly affected by energy losses. Figure 4.7 presents the ratio of the pressure gradient to the gravity force as a function of distance from the center of the starburst. At the stagnation radius $dP/dr = F_g$ (see equation [2.8] in Chapter 2) and thus the

intersection of lines which display this ratio with the thin horizontal line marks the position of the stagnation point for various cases. Figure 4.7 panel (a) shows the ratio of the pressure gradient to the gravity force for starbursts with identical mass and radii (equal to those of model 2c in Table 4.1) when the thermalized gas was assumed to have different metallicities. In these cases the displacement of the stagnation radius to larger and larger values is promoted by the increasingly larger amount of energy lost through radiative cooling within the considered starburst. Similarly, radiative cooling is enhanced as one considers more massive starbursts. These reinsert more material per unit time and thus lead to a more significant radiative cooling, as shown in Figure 4.7 panel (b), for cases 2c and 2e. In the region $r < R_{st}$, the outward pressure gradient is not able to compensate the gravity force and then all matter reinserted within the stagnation volume falls towards the central SMBH. On the other hand, in the region $R_{st} < r < R_{NSB}$ the pressure gradient exceeds the gravity force and hence the matter deposited there accelerates outwards and conforms a supersonic wind. Similar trends were noticed in the 3D results of Schartmann et al. (2009) when considering the mass and energy input rate from planetary nebulae and type I SN in evolved clusters surrounding a SMBH. Here however, we conclude that the amount of matter which fuels the central SMBH and that which forms the starburst wind, both depend directly on the location of the stagnation radius. This section is focused on the

properties of the bimodal flow in the catastrophic cooling regime, thus the resultant values for R_{st} , accretion rates, and the associated SMBH luminosities for the models given in Table 4.1 are presented in Section 4.5.

4.3.4 The structure of the bimodal flow in the catastrophic cooling regime

Figure 4.8 shows the results of numerical simulations for massive starbursts with strong radiative losses (models 2e, 2g and 2h). Here the upper, middle and lower panels present the quasi-stationary distribution of the flow velocity, density and temperature, respectively. As one considers more energetic (or more massive) starbursts, the larger densities (see middle panels) promote a faster radiative cooling within the thermalized plasma and this results in a smaller pressure gradient and thus in a further displacement of the stagnation radius towards larger distances from the starburst center. This is shown by vertical dotted lines in the upper panels. The structure of the accretion flow for starbursts in the catastrophic cooling regime presents some distinct features. In particular, the temperature distribution is different from that in the case of starbursts in the quasi-adiabatic regime. It drops smoothly within the starburst region until a thermal instability develops within the accretion flow. The temperature then suddenly drops to the minimum permitted value (10^4 K), as shown in the bottom panels

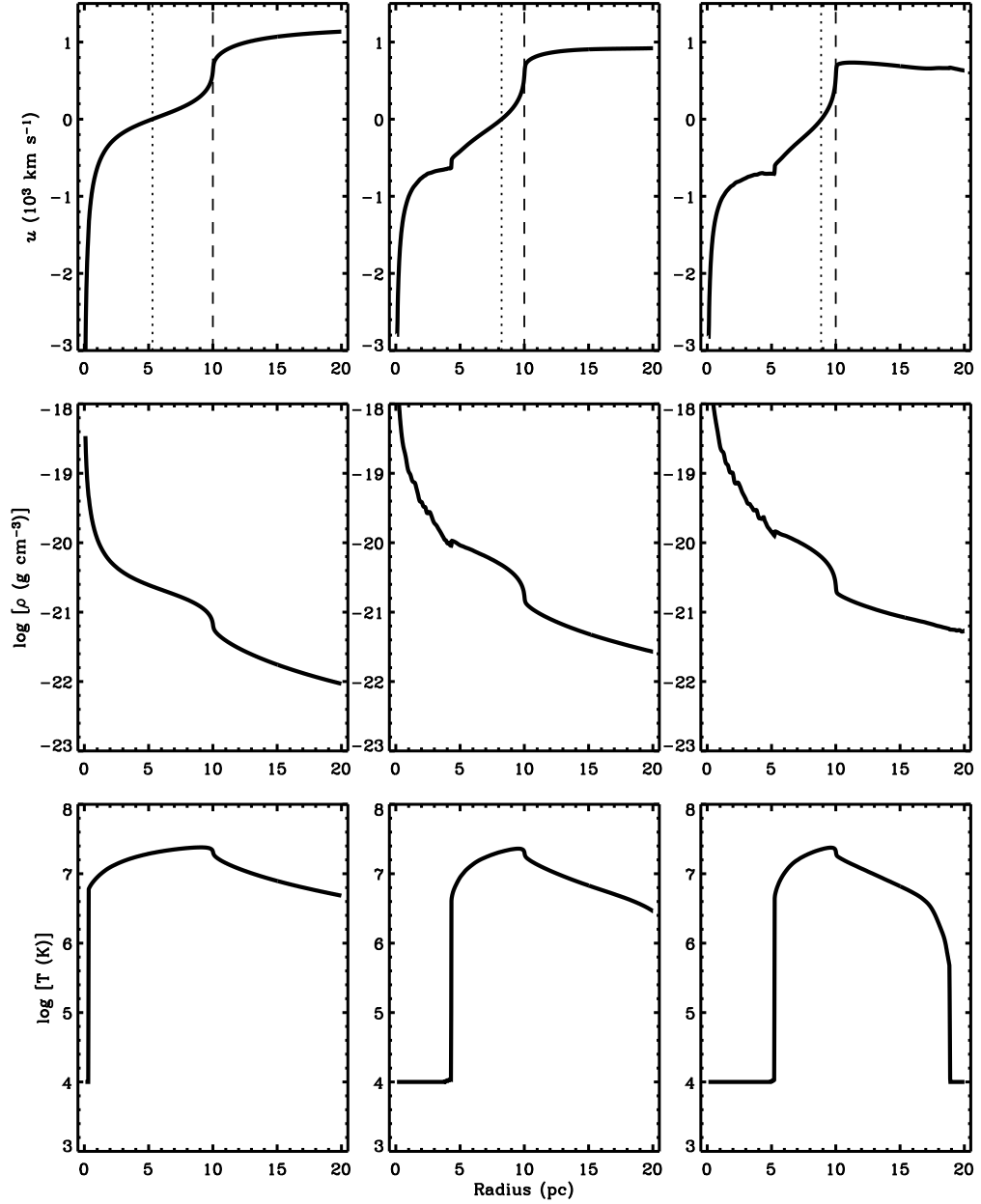


Figure 4.8: The bimodal solution for NSBs with $L_{NSB} > L_{crit}$ and a central SMBH. Panels from left to the right correspond to models 2e, 2g and 2h, respectively. Upper, middle and lower panels display the stationary velocity, density and temperature distributions, respectively. Dotted and dashed lines in the upper panels mark the location of R_{st} and R_{NSB} , respectively. R_{st} is larger for more energetic starbursts, because the strong radiative cooling depletes more rapidly the temperature. The thermal instability occurs also at a larger distance from the center.

in Figure 4.8, and the accretion flow remains at the ionization temperature despite the continuous input of energy in that region. As a consequence the accretion flow is supersonic in the catastrophic cooling regime, see Figure 4.5, and Figure 4.9 for the case 2f in Table 4.1. Note that the thermal instability appears at larger distances from the center as one considers a larger mass deposition rate or a more massive and luminous starburst (Figure 4.8, bottom panels). However, in all cases the cold and supersonically in-falling flow is well restricted to the central regions of the starburst, well within the stagnation volume. This is the reason why the semi-analytic method is able to find with great accuracy the location of the stagnation point, even for starbursts above the threshold line.

Faster cooling leads also to a smaller wind speed. If one measures at a distance $r = 2R_{NSB}$ it is 1136 km s^{-1} in the less energetic considered model (2e) and 629 km s^{-1} in the most energetic case (model 2h), instead of the 1500 km s^{-1} expected in the adiabatic case. Note that for the most energetic case (model 2h), the temperature drops also suddenly to 10^4 K in the free-wind region.

At this point we can summarize the properties of the hydrodynamic solution of the injected gas by the massive members of nuclear starbursts with a central SMBH by the following scenario: if the starburst is in a quasi-adiabatic regime (low mass clusters) the stagnation radius is small and the accretion flow is subsonic. As one considers

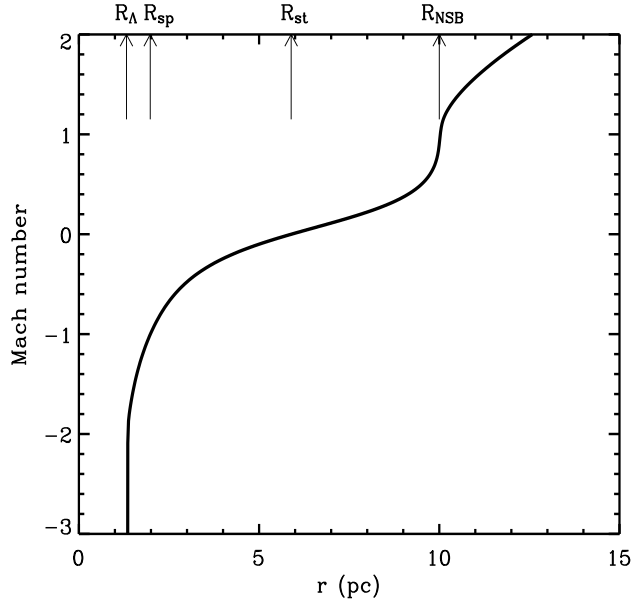


Figure 4.9: Structure of the bimodal flows in the catastrophic cooling regime. Here in terms of the Mach number we show that in the catastrophic cooling regime the accretion flow (defined by the matter deposited within R_{st}) becomes supersonic at R_{sp} and then experiments a thermal instability at a radius, R_{Λ} , interior to the *inner* sonic point. R_{Λ} , R_{sp} , and R_{st} move toward the nuclear starburst edge R_{NSB} when one considers more energetic starbursts. The calculations were performed for model 2f presented in Table 4.1.

more massive clusters radiative cooling becomes more important and the accretion flow is transonic, the transition from subsonic to supersonic inflow velocities occurs between the stagnation radius and the cluster center, at a large distance from the last stable orbit used in section 4.2 as the position of the *inner* sonic point. Finally, if the nuclear starbursts evolves in the catastrophic cooling regime the accretion flow experiments a thermal instability (see Figure 4.8) at a radius interior to the *inner* sonic point. In this more general case the configuration

inside the starburst volume is $0 < R_\Lambda \leq R_{sp} < R_{st} < R_{NSB}$, where R_Λ is the radius at which the thermal instability occurs and R_{sp} the distance at which the special point sets in (equal to the *inner* sonic point), see Figure 4.9. All these radii move out toward the cluster edge as one considers more and more massive clusters.

4.3.5 Impact of the supermassive black hole mass on the bimodal flow

Figure 4.10 shows the impact of the SMBH mass on the bimodal flow for a nuclear starburst whose parameters are the same as in model 2f but considering different masses for the central black hole $M_{SMBH} = 10^6 M_\odot$, $10^7 M_\odot$, and $10^8 M_\odot$, presented by dotted, dashed, and solid lines, respectively. Note that even if the black hole mass spans two orders of magnitude, the position of the stagnation point sets in almost at the same radius and the wind flow remains almost unchanged. In this case radiative cooling defines where the stagnation point lies. The main difference occurs in the profiles of the accretion flow where the injected matter accelerates faster towards the center in the case of the more massive black hole (solid line) and the thermal instability, which coincides with the sudden change in velocity, appears at a smaller distance from the center.

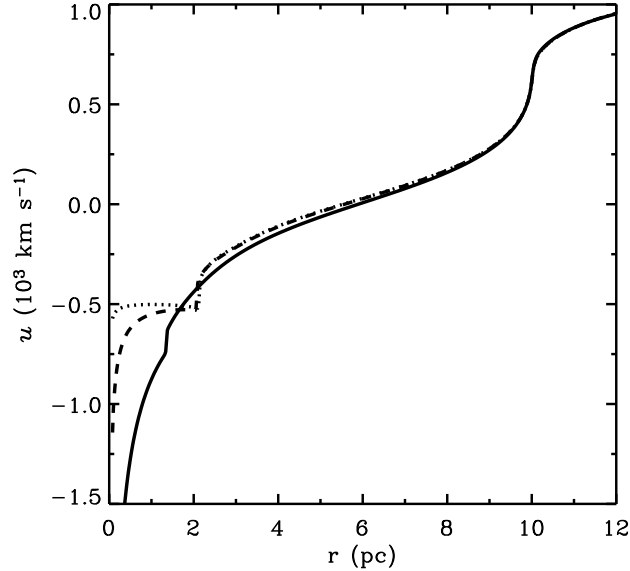


Figure 4.10: Impact of black hole mass on the accretion flows. The velocity profiles for the bimodal flows that results from the injected matter by a nuclear starburst of mass $M_{NSB} = 2.75 \times 10^8 M_{\odot}$ with different central black holes: $M_{SMBH} = 10^6 M_{\odot}$, $10^7 M_{\odot}$, and $10^8 M_{\odot}$, here presented by the dotted, dashed, and solid lines, respectively. Here the stagnation point is defined mainly by the radiative cooling. The impact of the SMBH is evident in the inner region of the accretion flow where gas moves faster toward the center as one considers more massive black holes. The location of the thermal instability, here shown as a sudden acceleration of the inflow, is less sensitive for low mass black holes and it occurs at a smaller radius in the more massive SMBH.

4.3.6 Impact of the minimum temperature allowed on the accretion flow

All simulations presented above use the ionization temperature $T = 10^4$ K as the minimum temperature at which the gas may cool down. However, if the ionizing photons are not sufficient to maintain ionized the

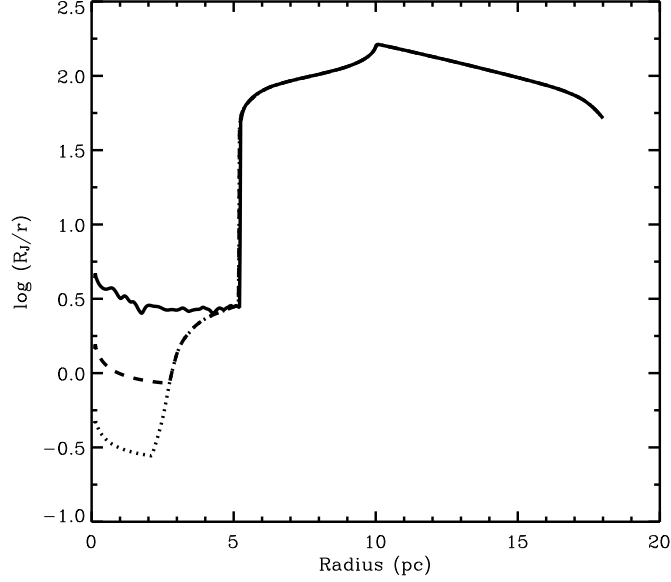


Figure 4.11: The ratio of the Jeans radius to the radius of the flow as a function of the distance to the nuclear starburst center in the case of model 2h. The flow is gravitationally unstable if $R_J < r$. The solid, dashed and dotted lines present $\log(R_J/r)$ for different minimum temperatures allowed in the calculations: $T_{min} = 10^4$ K, 10^3 K and 10^2 K, respectively. The accretion flow becomes gravitationally unstable if the temperature may fall below 10^3 K.

high density gas, this matter may cool down to lower temperatures leading the possibility for the accretion flow to be gravitationally unstable. Figure 4.11 presents the Jeans radius, $R_J = 0.5c_s(\pi/G\rho)^{1/2}$ (Clarke and Carswell, 2007), where c_s is the local sound speed calculated at each r inside the stagnation volume for the most massive model 2h, in Table 4.1. R_J would be larger than r if the central SMBH or the starburst are able to photoionize the accretion flow and the gas temperature cannot drop below 10^4 K. However R_J may be smaller than r , and

thus the accretion flow may become gravitationally unstable if the temperature falls below 10^3 K (e.g. Wada et al. 2009). However, note that the stagnation radius does not depend on the minimum temperature allowed in the calculations.

4.4 The bimodal flow in the gravitationally bound regime

As was shown in previous sections the hydrodynamic solution depends on where the system is located in the parameter space $R_{NSB} - L_{NSB} - M_{SMBH}$, and thus the bimodal solution is determined by the location of the stagnation point which is well fixed by the balance between the gravity force and the thermal pressure. The thermal pressure is strongly affected by radiative losses of energy and in very massive and compact nuclear starbursts hosting a central SMBH, the gravity force wins over the outward directed pressure gradients. In this case the stationary solution does not exist and eventually all mass returned inside the starburst falls towards the center, this is what we call the gravitationally bound regime. This regime is located to the left of the critical radius marked by the dashed line in Figure 4.1.

In this case the hydrodynamic solution presents many features. Figure 4.12 displays in panels (a), (b), and (c) the runs of velocity, temperature, and density, respectively. Different colors correspond to

four snapshots in the simulation $t = (23.8, 25.4, 27.0, 28.6) \times 10^3$ yr presented in black, blue, green and red colors, respectively. The simulation was performed for a very compact ($R_{NSB} = 1$ pc) and massive ($M_{NSB} = 1.5 \times 10^8 M_{\odot}$) nuclear starburst with a central $10^8 M_{\odot}$ black hole. In this case the stagnation radius is close to the star cluster edge and the outward pressure gradient is not able to produce a starburst wind, see panel (a), and eventually all the injected matter goes toward the center. In this case the high density of the matter reinserted promotes a fast cooling of the thermalized gas and thus leads to the formation of thermal instabilities inside and outside the starburst volume, where temperature drops to the minimum value allowed in the calculations, see panel (b). The thermal instabilities favor the formation of density peaks outside the cluster volume by squeezing the cold gas with the hot surrounding medium, see the density profiles in panel (c). The spike in density formed outside the cluster volume moves toward the starburst edge because of gravity and finally falls toward the center together with all the reinserted matter, then a new cycle restarts. As was pointed out in Chapter 3 this type of solution has little impact on the surrounding interstellar medium but instead it results into a positive feedback condition which may contribute to the formation of new stars within the cluster volume.

Figure 4.13 displays the solution for a model presented by Schartmann et al (2009) in their 3D model. They assume that massive stars

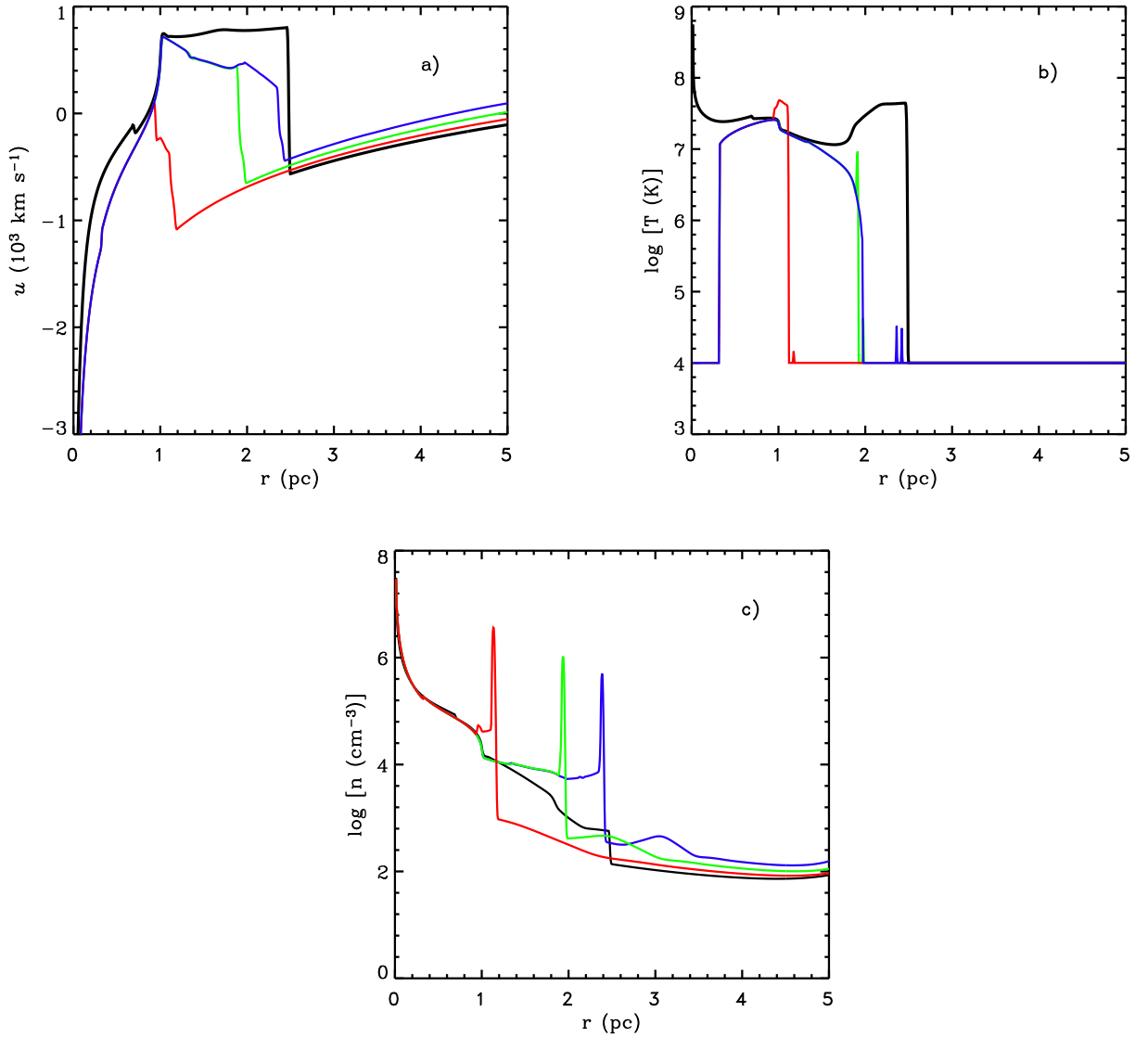


Figure 4.12: The gravitational bound regime in the case of a nuclear starbursts with a central supermassive black hole. Panels (a), (b), and (c) show the velocity, temperature, and number density profiles, respectively. The black, blue, green and red lines corresponds to four evolution times $t = 23.8, 25.4, 27.0,$ and 28.6 thousand years, respectively. In this case the outward pressure gradient is not able to form a wind. The strong radiative cooling promotes the formation of thermal instabilities and in this particular case, the formation of a dense shell outside the cluster volume which eventually falls to the center with all the injected matter.

and type II supernova take away all the reinserted matter (the present work shows that this is not the case and even more, the combination of gravity and radiative losses may result in a positive feedback condition). Their study considers only the matter left over by type I supernovae and planetary nebulae. In this respects our results are complementary. Here by means of 1D simulations with the parameters extracted from Schartmann et al. (2009) we found that their solution is in a gravitationally bound regime. The calculations were performed for a star cluster mass $M_{NSB} = 6.7 \times 10^8 M_{\odot}$, radius $R_{NSB} = 25$ pc, mechanical luminosity $L_{NSB} = 2.12 \times 10^{41}$ erg s⁻¹, adiabatic wind terminal velocity $V_{A,\infty} = 411$ km s⁻¹, minimum temperature T=10 K, and a central super massive black hole of mass $M_{SMBH} = 6.6 \times 10^7 M_{\odot}$. In Figure 4.13 the velocity, temperature and density distributions are displayed with black, red, and blue lines, respectively. Note that in this snapshot ($t = 0.2$ Myr) the stagnation point is close to the cluster edge, see black line. One can observe a multiphase interstellar medium: cold and high density shells formed by thermal instabilities and enhanced by shocks, and hot gas moving all together toward the center. The cold and high density gas observed across the space could resemble the cold clumps observed in Schartmann et al. (2009).

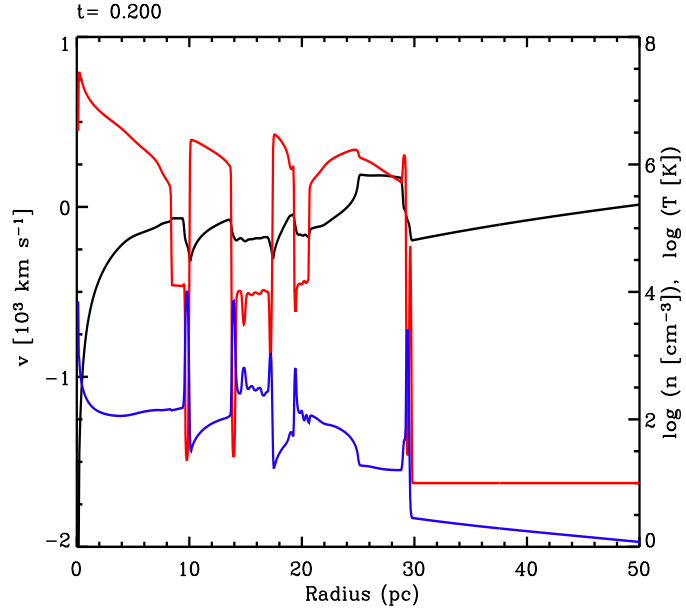


Figure 4.13: Multiphase interstellar medium in the gravitational bound regime. Here velocity, temperature and number density profiles are displayed in black, blue and red colors, respectively. The calculations were performed with parameters extracted from Schartmann et al. (2009) and they are given in the text. One can observe multiple high density shells (in blue) at low temperatures (in red) produced by thermal instabilities and shocks driven by the hot surrounding medium onto low temperature gas. Note the complex velocity pattern (in black) inside the cluster volume due to the formation of shocks. One can observe a multiphase gas whose temperature ranges from 10 K to $\sim 10^7$ K, with density differences of more than two orders of magnitude.

4.5 The SMBH accretion rate and luminosity, and the power of the NSB super wind

The hydrodynamic solution discussed in the previous sections allows one to calculate the accretion rate and thus the SMBH luminosity for each model presented in Table 4.1 which includes models in the

quasi-adiabatic and the catastrophic cooling regimes. The results of the calculations are summarized in Table 4.2. Where, Column 1 is a reference to the model, Column 2 presents the resultant stagnation radius. The total mass deposition rate is shown in Column 3 and should be compared with the resultant accretion rate and the mass outflow in the starburst wind, presented in Columns 4 and 5, respectively. Column 6 shows the SMBH luminosity normalized to the Eddington limit ($L_{Edd} = 1.3 \times 10^{38} M_{BH} M_{\odot}^{-1} \text{ erg s}^{-1}$). The ram pressure of the outflow at the starburst edge ($P_{ram} = \rho u^2$) is presented in Column 7.

The time-dependent accretion rates for models 2c-2f calculated as the mass flux through the inner grid boundary are shown as examples in Figure 4.14. At $t = 0$ Myr, the accretion rate, \dot{M}_{acc} , is equal to zero because a stationary wind solution with $R_{st} = 0$ was used as the initial condition. However, the accretion rate grows rapidly and reaches the stationary level of $0.14 M_{\odot} \text{ yr}^{-1}$, $0.59 M_{\odot} \text{ yr}^{-1}$ and $1.36 M_{\odot} \text{ yr}^{-1}$ for models 2c, 2d and 2e, respectively. Note that the accretion rates grows due to the larger stagnation volume and the larger mass deposition rate from more massive starbursts. After a small relaxation time ~ 0.1 Myr, the solution becomes quasi-stationary and the total mass is conserved $\dot{M}_{NSB} = \dot{M}_{acc} + \dot{M}_w$; see Table 4.2 (Columns 3-5, respectively). Consequently, the fraction of the deposited matter expelled as super winds from the starbursts region decreases for more energetic starbursts although in absolute values it grows with the mass

Table 4.2: The predicted accretion rate and the power of the wind

Model	R_{st}	\dot{M}_{NSB}	\dot{M}_{acc}	\dot{M}_w	L_{acc}/L_{Edd}	P_{ram}
	(pc)		($M_{\odot} \text{ yr}^{-1}$)			($10^{-7} \text{ dyn cm}^{-2}$)
(1)	(2)	(3)	(4)	(5)	(6)	(7)
1a	2.1	8.45	1.88×10^{-3}	8.44	8.2×10^{-4}	1.96
1b	4.7	16.89	4.33×10^{-2}	16.86	1.9×10^{-2}	3.82
1c	11.4	25.34	0.93	24.72	0.4	5.39
1d	14.4	28.72	1.38	27.33	0.6	5.89
1e*	17.5	33.79	2.88	30.89	1.2	6.57
2a	1.3	1.27	5.09×10^{-3}	1.26	2.2×10^{-3}	4.66
2b	1.7	2.11	1.02×10^{-2}	2.07	4.5×10^{-3}	7.67
2c	2.8	4.22	0.14	4.09	6.1×10^{-2}	14.64
2d	4.4	7.03	0.59	6.45	2.6×10^{-1}	22.07
2e	5.3	9.38	1.36	8.00	0.6	26.83
2f*	5.9	11.61	2.38	9.23	1.04	30.53
2g*	8.2	42.23	23.28	18.74	10.2	56.16
2h*	8.9	84.46	59.54	25.48	26.0	77.43

The predicted accretion rate and the power of the wind. Column 1 is a reference to the models presented in Table 4.1. The results of the calculations: the value of the stagnation radius (R_{st}), total starburst mass deposition rate (\dot{M}_{NSB}), the calculated mass accretion rate (\dot{M}_{acc}), the rate at which matter flows away from the starburst as a super wind (\dot{M}_w), the stationary SMBH accretion luminosity normalized to the Eddington limit (L_{acc}/L_{Edd}) and the ram pressure of the wind (P_{ram}) are shown in Columns 2 to 7, respectively. * symbols mark those models for which the accretion luminosity exceeds the Eddington limit.

of the considered starburst (see Table 4.2).

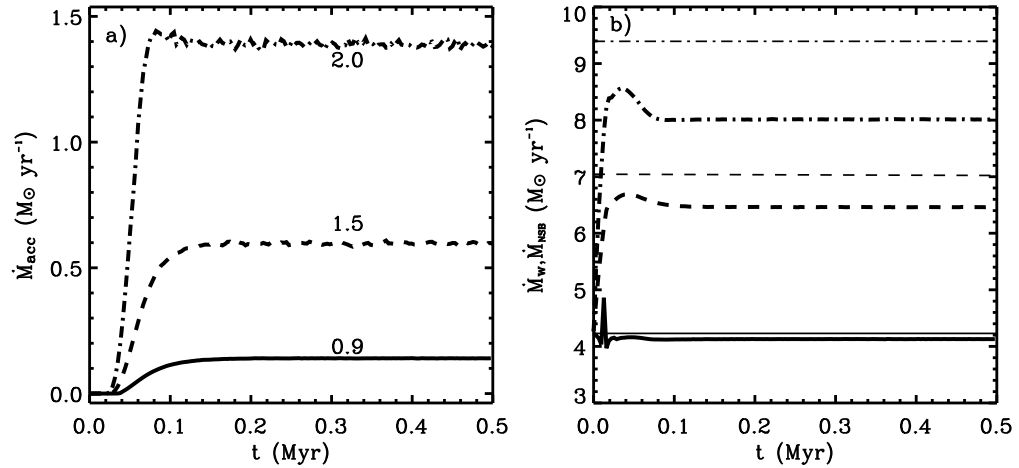


Figure 4.14: The balance of mass in the starburst region. Panel (a) shows the accretion rate onto the central $10^8 M_{\odot}$ black hole for models 2c, 2d and 2e -solid, dashed and dash-dotted lines, respectively. The labels indicate the L_{NSB}/L_{crit} values. Panel (b) displays the total mass deposition rate (thin lines) and the mass that streams away from the starbursts as a superwind, for the same models.

The stationary accretion rates onto the SMBHs, \dot{M}_{acc} , and the stationary rate at which matter is ejected as a starburst wind, \dot{M}_w , obtained through the numerical integration of the flow equations and normalized to the total mass deposition rate, \dot{M}_{NSB} , are shown in Figure 4.15 panel (a) as a function of the normalized starburst mechanical luminosity, L_{NSB}/L_{crit} . The circles represent the results from the numerical simulations of models 2a-2e. The solid and dashed lines present the semi-analytic \dot{M}_{acc} and \dot{M}_w , respectively, calculated according to equation [4.1]. The mass accretion rate onto the SMBH grows more

rapidly when the starburst mechanical power exceeds the critical value, ($L_{NSB} > L_{crit}$), as shown in Figure 4.15, panel (b). This leads to a rapid increase in the central SMBH luminosity, $L_{acc} = \eta_{acc} \dot{M}_{acc} c^2$ (where $\eta_{acc} = 0.1$ is the accretion efficiency and c is the speed of light) which approaches rapidly to the Eddington limit. There, the open circles result from our numerical simulations, the solid and dotted lines present the semi-analytic results for starburst with $R_{NSB} = 10$ pc (models 2a-2e; see Table 4.1), and $R_{NSB} = 40$ pc (models 1a-1d), respectively. The cross symbols mark the critical luminosity value ($L_{NSB} = L_{crit}$). Note, that the accretion rate and the SMBH luminosity obtained numerically are in a good agreement with those predicted by the semi-analytic model, even for starbursts with $L_{NSB} > L_{crit}$. This implies that the semi-analytic calculations lead to the correct value of the stagnation radius and thus may be used to estimate both the starburst wind power and the accretion onto the central SMBH and its corresponding luminosity in both the quasi-adiabatic and the catastrophic cooling regime.

Note that in both sets of calculations (R_{NSC} equal to 10 pc and 40 pc, with the assumed $V_{A,\infty} = 1500$ km s⁻¹) the accretion rate reaches values ~ 1.4 M_⊙yr⁻¹ when $L_{NSB} \sim 2L_{crit}$, see Table 4.2. This could result in $\sim 50\%$ increase in the mass of the SMBH after ~ 50 Myr. Note also that the calculated accretion luminosity exceeds the Eddington limit when the starburst mechanical luminosity is just about twice its

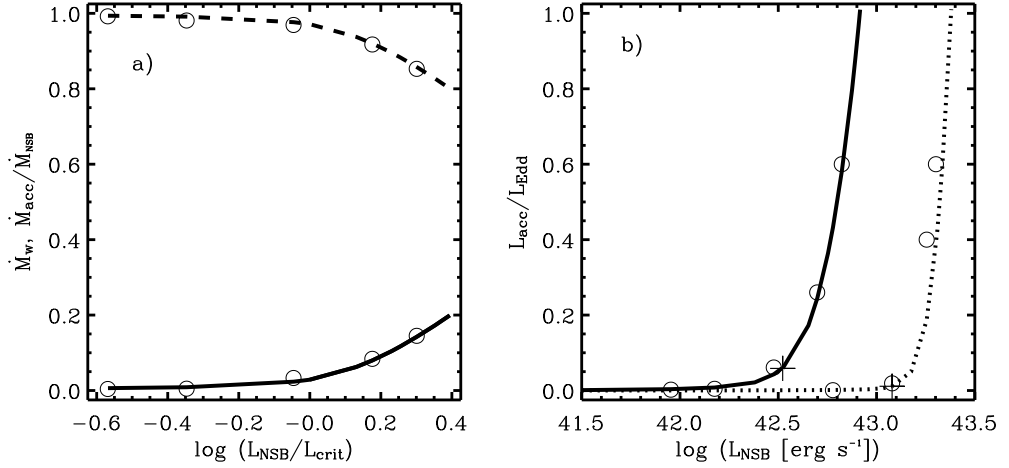


Figure 4.15: Predictions for the accretion rate and SMBH luminosity. Panel (a) presents the calculated mass accretion rate (lower circles) and the rate at which mass is expelled as a superwind (upper circles) from the simulations for starbursts below and above the threshold line (models 2a-2e). These are compared with the semi-analytic predictions for \dot{M}_{acc} and \dot{M}_{wind} , solid and dashed lines, respectively. All rates have been normalized to the total starburst mass deposition rate, \dot{M}_{NSB} . Panel (b) shows the SMBH luminosity normalized to the Eddington limit for models whose accretion luminosity does not exceed L_{Edd} , see Table 4.2. The circles represent results from the numerical simulations, solid and dotted lines show semi-analytic calculations for starburst with 10 pc (models 2a-2e) and 40 pc (models 1a-1d), respectively. An accretion efficiency of $\eta_{acc} = 0.1$ was used in the calculations. Cross symbols represent starbursts with the critical energy (L_{crit}) input rate.

critical luminosity, see Table 4.2, models 1e, 2f-2h. The calculated \dot{M}_{acc} and L_{acc} must be considered as upper limits because here we do not consider additional physics which could result in lower values for these quantities, see Chapter 6.

Certainly, the accretion rate and hence the SMBH luminosity could be reduced if additional physics are included in the model. For example, one could think on a 2D or 3D geometry that could account for

the radiative and/or mechanical feedback from the central AGN and the redistribution of the net angular momentum in the accretion flow (e.g., Schartmann et al. 2009). However, our 1D model accounts for a realistic deposition of mass and energy around a central SMBH, and hence the results here presented give a good estimate of the accretion rate upper limit. And more important of all, the model establishes a direct interplay between nuclear starbursts and their central SMBHs. A direct interplay in which all the reinserted matter unable to join the superwind, becomes available to the SMBH. The starburst wind, on the other hand, could be sufficiently powerful to significantly re-structure the host galaxy ISM, leading perhaps to a thick ring, along the plane of the galaxy, and to a supergalactic wind along the host galaxy symmetry axis (as in Tenorio-Tagle & Muñoz-Tuñón 1997, 1998).

A simple estimate of the wind power can be obtained from its ram pressure (P_{ram}) at the starburst edge, see column 7 in Table 4.2. This is, in all cases, many orders of magnitude larger than the typical ISM pressure in our Galaxy ($\sim 10^{-12}$ dyn cm⁻²). It also exceeds by almost three orders of magnitude the pressure exerted by a one particle per cubic centimeter ISM, freely falling onto the starburst ($P_{ISM} = \rho_{ISM} v_{ff}^2$) with $v_{ff} = [2G(M_{BH} + M_{NSB})/R_{NSB}]^{1/2}$. The implication is that the resultant winds are to lead to the build up of superbubbles and probably to supergalactic winds, preventing, in most cases, the falling of the ISM onto the nuclear starburst. Perhaps only in the case of an extremely

dense ISM ($\rho_{ISM} \sim 10^{-20} - 10^{-21} \text{ g cm}^{-3}$) freely falling onto the central starburst would modify the structure of the outflow and of the accretion flow. This latter possibility is out of the scope of this thesis.

4.6 X-ray emission from the accretion flow

The matter reinserted and thermalized inside the starburst region may contribute to the observed X-ray emission. The 0.2 - 8.0 keV X-ray luminosity from the whole computational domain can be estimated by using equation [3.4] presented in Chapter 3. In this case the integral limits are the inner and outer boundaries of the computational domain, R_{min} and R_{max} . This is equal to about $2.5 \times 10^{41} \text{ erg s}^{-1}$ and $2 \times 10^{42} \text{ erg s}^{-1}$ for cases 2c and 2e in Table 4.1, respectively. The X-ray luminosity of the in-falling matter is even smaller, it is about $\approx 3.9 \times 10^{40} \text{ erg s}^{-1}$ and $1 \times 10^{42} \text{ erg s}^{-1}$, respectively. This emission is orders of magnitude smaller than the SMBH luminosity, which is $L_{acc} \approx 8 \times 10^{44} \text{ erg s}^{-1}$ in case 2c and $L_{acc} \approx 8 \times 10^{45} \text{ erg s}^{-1}$ in case 2e, if the accretion efficiency is as usual set $\eta_{acc} = 0.1$. Thus, it would be hard to detect the infalling matter contribution to the total X-ray emission. In this case, low luminosity AGNs seem to be better candidates to show the infalling matter X-ray emission, as in the case of the Seyfert 2/LINER galaxy NGC 4303. This shows the Raymond-Smith soft X-ray emission ($kT \approx 0.65 \text{ keV}$) originating in the core of the galaxy with $r \leq 15 \text{ pc}$,

coincident with a young (age around 4 Myr, and a 3 pc radius), nuclear super star cluster (see Jimenez-Bailon et al. 2003).

4.7 Conclusions

By means of 1D numerical simulations and semi-analytic calculations, we have worked out the hydrodynamic solution for the matter reinserted by stellar winds and type II supernovae from a young, massive and compact starburst in presence of a central SMBH. The solution is bimodal in all cases, with a stagnation radius (R_{st}) which defines the outer boundary of the accretion flow onto the SMBH as well as the inner boundary of the starburst wind. There are three possible hydrodynamic regimes: the quasi-adiabatic regime in the case of low mass starbursts with subsonic accretion flows and small accretion rates onto the SMBH, the catastrophic cooling regime for massive NSBs with supersonic accretion flows and high accretion rates for the black hole, and the gravitationally bound regime in the case of very massive and compact NSBs in which eventually all the injected matter by the NSB remains bound within the starburst volume and falls toward the center leading to the possibility of a positive feedback condition.

We have shown that outside the gravitationally bound regime, at the stagnation radius the gravity force perfectly balances the outward pressure gradient acquired by the thermalized reinserted matter. We

have also shown that radiative cooling becomes an important issue for massive starbursts with a mechanical luminosity above the threshold line ($L_{NSB} > L_{crit}$). In all these cases, radiative cooling depletes the pressure established through thermalization of the injected matter and this leads to the development of a thermal instability in the accretion flow. The stagnation radius then moves rapidly, towards the starburst boundary, with the mass of the considered starburst. In all simulations with $L_{NSB} > L_{crit}$, strong radiative cooling occurs at a radius interior to the stagnation radius. Radiative cooling re-structures the inner accretion flow lowering the temperature to the minimum allowed. From then onwards and despite the continuous input of energy, the rapid velocity increase leading to a rapid density enhancement keeps and sustains the in-falling gas at the ionization temperature. It is the larger mass deposition rate, provided by more massive starbursts, what triggers the onset of strong radiative cooling and with it the shift of the stagnation radius towards the starburst boundary. This results in a rapid increase of the central SMBH luminosity for starbursts further above the critical threshold in the $L_{NSB} - R_{NSB} - M_{BH}$ parameter space, approaching rapidly to the Eddington limit. The larger mass deposition rates provided by more massive starbursts also leads to more powerful starburst winds and an estimate of their mechanical power rules out the possibility of the ISM feeding the SMBH, at least during the type II supernova era. However, in the case of very compact and massive starbursts we ob-

serve the formation of multiple thermal instabilities and shocks in the outflow as well as in the inflow, and eventually the gravity force wins over the outward pressure gradients and thus in this case the solution is not stationary. This results in a positive feedback condition in which all the matter injected by the NSB remains bound within its volume and may favor the formation of a new generations of stars. This type of solution has little impact on the ISM outside the cluster volume.

Clearly, spherically symmetric calculations, as the ones presented here, cannot account for the redistribution of the net angular momentum in the accretion flow. Nevertheless, they provide a good estimate of the upper limit to the accretion rate onto the central black hole, while pointing to a direct physical link between nuclear starbursts and the central SMBH luminosity. Our calculations do realistically account for the symmetric deposition of mass and energy from massive stars around the central object. This suggests that in a more realistic 2D or 3D geometry, able to account for the redistribution of the net angular momentum, the hydrodynamics would still lead to a bimodal solution with an accretion flow and an outward wind. In such a case however, the residual angular momentum could favor the formation of a gaseous disk well contained within the nuclear starburst region.

Chapter 5

Conclusions

Main conclusions of this thesis

By means of semi-analytic calculations and 1D numerical simulations, this thesis presents a detailed study of the hydrodynamics of the gaseous flows driven by star-forming regions: a galaxy as a whole, and nuclear starbursts at the center of active galaxies. A self-consistent set of equations was used in order to account for the major physical processes involved in such phenomena: sources of mass and energy, radiative losses, and the gravity pull from the system. The first part of the dissertation studied the hydrodynamics of the matter reinserted by young assembling galaxies. In this case, continuous star formation was considered for the starburst model. The second part of this thesis was dedicated to the study of the interplay between nuclear starbursts and super massive black holes. In this case an instantaneous starburst was assumed.

Part I

In the first part we realize that there are three major hydrodynamic regimes: the wind solution, the bimodal solution and the gravitationally bound solution. Which solution takes place depends on the rate of star formation, the protogalaxy total mass and its size, and the rate of mass loading from protostellar clouds. Here we understand that in the case of large galaxies with low star formation rates and small ablation coefficient, the stagnation radius is located at the center of the cluster and thus the high pressure, generated by thermalization of the reinserted matter within the protogalaxy, produces supersonic winds which carries away the matter returned by massive stars and that ablated from protostellar clouds. In the case of massive protogalaxies radiative losses of energy becomes an important agent, mainly in the central regions of the galaxy, and depletes the pressure in the inner zones, thus the stagnation point moves out from the center. In this case the flow is bimodal, with mass accumulation within the stagnation radius and a wind flow generated by the matter reinserted between the stagnation volume and the star-forming edge. Finally, in the case of very compact and massive assembling galaxies, the gravitational force wins over pressure gradients and in such cases all the injected and ablated matter is retained within the protogalaxy volume. In this case the model predicts a small impact of the young galaxy on the intergalactic medium. The

main conclusion of this study is that the combination of gravity and high star formation rates may result in a positive feedback condition which may induce new generations of stars and metal enrichment of the forming galaxy.

Part II

In the second part of this thesis we found that there are also three hydrodynamic regimes for the gaseous flows driven by nuclear starbursts with a central supermassive black hole: the quasi-adiabatic solution for low mass (energy) starbursts, the catastrophic cooling regime for massive bursts, and the gravitationally bound regimes in the case of compact and massive starbursts. Nevertheless, in this case the solution is always bimodal because the gravity pull from the central black hole prevents the injected matter to escape from the central region and thus the stagnation point is out of the center. Here the position of the stagnation point is well defined by the balance between gravity force and pressure gradients. In the case of low mass starbursts hosting a central black hole, the hydrodynamic solution presents a starburst wind and a subsonic accretion flow, with small accretion rates for the black hole. In this case the stagnation radius is defined mainly by the gravity of the super massive black hole. In the case of massive starbursts the radiative cooling is more important and depletes the temperature in the

central region of the cluster and thus promotes a faster displacement of the stagnation radius towards the cluster edge, and with this a fast increase of the amount of matter that is able to fuel the central black hole, approaching rapidly to the Eddington limit. Finally, in the case of compact and massive nuclear starburst with a central super massive black hole the solution is not stationary. Here the combination of gravity and strong radiative losses impede the formation of starburst winds and in such cases all the reinserted matter eventually remains bounded within the star cluster volume and falls toward the center. The main contribution of this study is that here we outline a direct physical connection between nuclear starbursts and super massive black holes. An interplay in which nuclear starbursts winds prevents the accretion of the ISM onto the central black hole and thus in this case the SMBH is fed with the matter re-inserted by massive stars and type II supernovae, instead of removing all gas from the star-forming region. And that in extreme cases the combination of strong gravity and catastrophic cooling may result in a positive feedback condition favoring to the formation of new generations of stars within the nuclear cluster, and thus in this last case a recurrent activity is envisaged. Next chapter discusses some key physical processes that will be considered in future projects.

Chapter 6

Physics to be considered in future projects

The results of this thesis leads to an intrinsic link between the luminosity of a SMBH located at the center of a young nuclear starburst and the starburst parameters. However, the model here developed still does not include some potentially important physical ingredients and thus requires further improvement. So far we have assumed that stars are equally distributed within the star-forming region. Therefore, a more realistic model for the stellar density distribution has to be developed, as it was suggested by some authors (see, Rodríguez-González et al. 2007) who have considered relatively low mass stellar clusters and presented the results without accounting for the impact of gravity provided by the stellar component and the presence of the central black hole.

Another major piece of physics, which has not been considered and

must be included into the model is the radiative feedback from the central SMBH (see, Ciotti et al. 2010 and references therein). This includes the photoelectric and Compton heating of the reinserted matter by the energetic photons from the central engine. In extreme cases this additional source of energy may be competitive with the stellar mechanical energy output in the starburst region and thus may change the position of the stagnation point and the accretion rate significantly. In the catastrophic cooling regime the radiative acceleration on dust may be also an important factor.

Another important issue is that the starburst mechanical luminosity and mass output rate are not constant, but change with the evolution of stars. This implies that the hydrodynamic regimes of the flow and thus the accretion rate onto the central SMBH might be functions of time. In the simplest approximations this requires a sequence of stationary models with different parameters taken from the starburst evolutionary synthesis model (e.g. Starburst99) to be considered as it is usually done in the theory of a single star evolution. Preliminary results by Silich et al. 2010 which take into consideration time evolution of starburst parameters, assuming an exponentially decaying star-formation rate, hint on the importance of mass loss from the intermediate mass (a few solar- $8 M_{\odot}$) stars at the end of the starburst event, as it is also suggested by the recent observational data (Davies et al. 2010). Thus a detailed study of the SMBH-starburst system time evolution should

be one of the major targets for future projects.

The metallicity of the matter reinserted by massive stars inside the starburst volume also changes drastically with time. This could have potentially a large effect on the dynamics of the reinserted matter and the accretion flow and lead to a fast metal enrichment of the interstellar gas, as observed in high redshift quasars (e.g., Hamann & Ferland 1999; Juárez et al. 2009). Thus changes in the reinserted gas chemical composition also must be considered.

There are two more input parameters which characterize the process of star formation that should be included in the model. These are the thermalization efficiency (see, Silich et al. 2007, 2009) and the mass ablation coefficient in the star-forming region (Silich et al. 2010). The thermalization efficiency is required in order to take into account that some fraction of the kinetic energy provided by massive stars are lost during the process of thermalization and thus does not participate in the hydrodynamics neither the wind nor the accretion flow. The mass ablation coefficient should be considered in the case of continuous star formation in order to account for the dispersion of the matter left over in the star formation process, see Chapter 3 for the case of SCUBA sources without a central SMBH.

All these possibilities mentioned above can be studied by using one-dimensional calculations. However, in order to have a more realistic constrain to the upper limit of the accretion rate onto the SMBH,

the model should include another important quantity: the net angular momentum of the accreting matter, and then study the impact of the redistribution of angular momentum on the SMBH activity. In this case, 2D and 3D models must be performed. In this respect, the formation of a gaseous disk (as observed in the results by Schartmann et al. 2009) interior to the starburst volume is expected, with a clumpy structure if catastrophic cooling sets in.

Thus a self-consistent model for the co-evolution of NSBs and SMBHs must includes most of the physical processes described above. This may let us understand the SMBH mass evolution in the starburst environment and may explain the fundamental relation between the central SMBHs and bulges of their host galaxies (Gebhardt et al. 2000; Ferrarese & Merritt, 2000), and also the correlation of SMBH luminosities with the nuclear SFR, observed for example by Chen et al. 2009.

Appendix A

The Eulerian hydro-code ZEUS

The ZEUS code is a time-explicit, Eulerian grid-based hydrocode which solves the fluid equations [2.1]-[2.3] by using the method of finite-differences and an operator split method (Stone & Norman 1992). The operator split method breaks the solution of the partial differential equations into parts, with each part representing a single term in the equations. The individual parts in the solution procedure are grouped into two steps, called the *source* and the *transport* steps. In the source step, the code solves finite-difference approximations to

$$\frac{\partial \rho}{\partial t} = q_m \tag{A.1}$$

$$\rho \frac{\partial \mathbf{u}}{\partial t} = -\nabla P - \rho \nabla \phi, \tag{A.2}$$

$$\frac{\partial e}{\partial t} = -P \nabla \cdot \mathbf{u}, \tag{A.3}$$

while in the transport step accounts for fluid advection by solving finite-difference approximations to the integral equations.

$$\frac{d}{dt} \int_V \rho dV = - \int_{dv} \rho(\mathbf{u} - \mathbf{u}_g) \cdot \mathbf{dS}, \quad (\text{A.4})$$

$$\frac{d}{dt} \int_V \rho \mathbf{u} dV = - \int_{dv} \rho \mathbf{u}(\mathbf{u} - \mathbf{u}_g) \cdot \mathbf{dS}, \quad (\text{A.5})$$

$$\frac{d}{dt} \int_V e dV = - \int_{dv} e(\mathbf{u} - \mathbf{u}_g) \cdot \mathbf{dS}, \quad (\text{A.6})$$

where \mathbf{u}_g is the grid velocity which allows for a moving grid.

ZEUS uses a staggered mesh so that scalars, and the individual components of vectors and tensors, are centered at different locations on the mesh. In general, scalars are stored at zone centers, while vectors are stored at the appropriate zone interfaces. There are two advantages to using a staggered mesh. The first is that vectors which are formed from differencing scalars are in a centered location between these scalars. Second, a staggered mesh reduces the number of interpolations needed for solving the advection equations [A.4]-[A.6] in the transport step. The active grid, on which the flow is evolved, is embedded in ghost zones, composed of two layers of ghost cells, which are necessary for providing boundary conditions.

In general, boundary conditions can be of two main types. In the *Dirichlet* condition, the value of a function, is prescribed on the boundary. In the *Neumann* condition, the derivative of the function normal to the boundary surface is prescribed. Common combinations of these

conditions are: reflecting, inflow, outflow, and periodic boundary conditions. Here we used outflow boundary conditions where all of the variables in the ghost cells are set to the corresponding values in the active cells.

There are two types of gridding. The first is rationed gridding where the distance across a zone is a fixed multiple of the distance across the previous zone. If this multiple is 1, then the zones are uniform. The second type of gridding is scaled gridding where the coordinate value is some fixed multiple of the previous coordinate value. The grid can be created all at once or in several blocks.

ZEUS uses a covariant formalism for differencing the dynamical equations. This allows to write the code in a coordinate-independent fashion by using the scale factors which describes the orthogonal coordinate system in which one would like to solve the equations. Thus ZEUS can be used for calculations in Cartesian, cylindrical, or spherical coordinates in one, two, or three dimensions. This is a very short description of the complex infrastructure of the hydrodynamic code ZEUS and the interested reader should revise the original series of papers by Stone & Norman (1992a,b); Stone, Mihalas & Norman (1992); and the book by Bodenheimer et al. (2007).

Appendix B

Impact of the inner grid boundary on the simulations

Here we analyze the effect of the assumed value of the inner grid cell on the hydrodynamic solution of the accretion flows presented in Chapter 4. The effect of the assumed value of the inner grid cell on the simulations was tested for various cases, in the quasi-adiabatic and in the catastrophic cooling regimes. Figure B.1, left panel, shows the impact of the inner grid cell on the accretion profiles in the case of a NSB with a central SMBH in the quasi-adiabatic regime. The simulations were performed for three values of the first grid zone: 0.1 pc, 0.05 pc and 0.01 pc, presented by the blue, red, and black trends in the left panel. Note that as one considers smaller values for the inner zone, the results from the simulations are closer to the semi-analytic solution, presented by the black line. Although, there is a discrepancy in the velocity profiles, note that the position of the stagnation point remains unchanged when

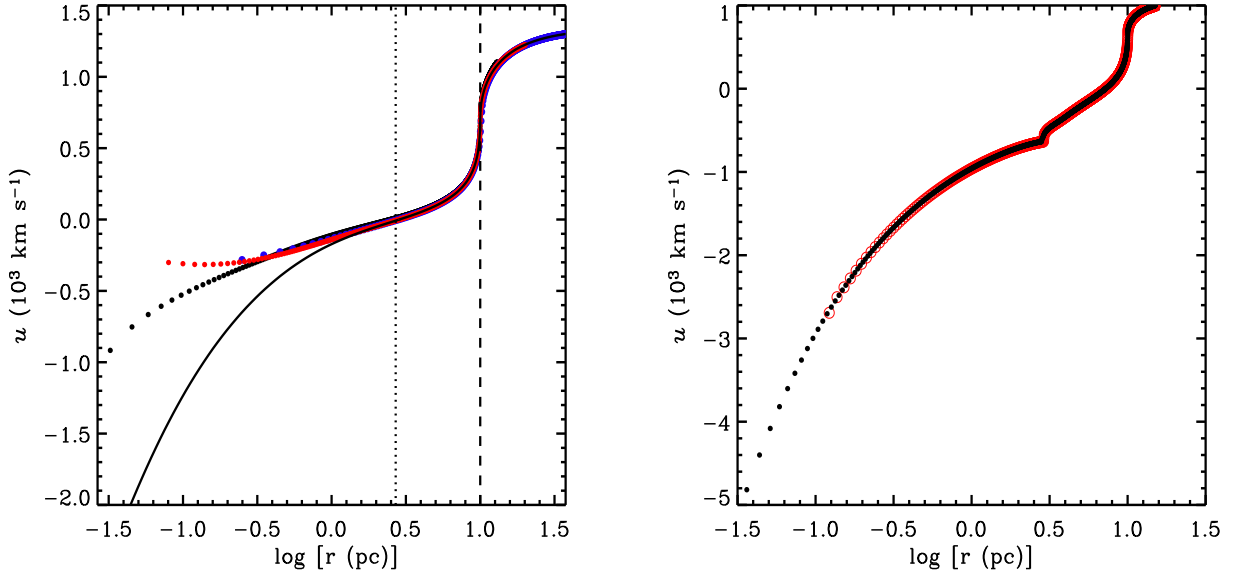


Figure B.1: Impact of the inner grid cell size on the accretion flow. The left panel presents the results from simulations for a model in the quasi-adiabatic regime. The runs were performed for values 0.5 pc, 0.1 pc, and 0.01 pc for the inner grid cell, they are presented by the blue, red, and black symbols, respectively. The numerical solution approaches the semi-analytic solution, presented by the solid line, in the case of a smaller inner zone. The stagnation radius (marked by the vertical dotted line) remains unchanged for the inner cell locations here used. The dashed line marks the starburst edge. Right panel presents the solution for a model in the catastrophic cooling regime. The red and black trends corresponds to the solution for two values of the inner grid zone, 0.1 pc and 0.01pc, respectively. In this case the two solutions are in excellent agreement across the space volume. The calculations were performed for a NSB of mass $M_{NSB} = 10^8 M_{\odot}$ (left panel) and $M_{NSB} = 5 \times 10^8 M_{\odot}$ (right panel), the black hole mass $M_{SMBH} = 10^8 M_{\odot}$ is the same in both cases. The radius of the NSB is assumed to be 10 pc.

one considers different (reasonable) values for the first grid cell. The effect of the inner grid zone is less important for models in the strong radiative cooling regime, see the right panel in Figure B.1. In this case the simulations were performed assuming the values 0.1 pc and 0.01 pc for the first zone, red and black trends respectively. Both solutions are in an excellent agreement. Thus both methods, the semi-analytic and full numerical simulations are complementary and they help us to find the complete hydrodynamic solution. The semi-analytic approach can be used to resolve the accretion flow in the quasi-adiabatic regime where very small values for the inner grid cell are required in the simulations in order to better resolve the accretion flow. Note that the time wasted in the simulations increases when one considers smaller values for the inner zone. On the other hand, full numerical simulations are required in order to find the complete hydrodynamic solution for models in the catastrophic cooling regime where the semi-analytic approach fails, and are essential to find the complex non-stationary solution in the case of the gravitationally bound regime.

Bibliography

- [1] Alexander, D. M., Bauer, F. E., Chapman, S. C., Smail, I., Blain, A. W., Brandt, W. N., & Ivison, R. J. 2005, *ApJ*, 632,736
- [2] Baumgardt, H. & Kroupa, P. 2007, *MNRAS*, 380,1589
- [3] Begelman, M. C., & Nath, B. B. *MNRAS*, 2005, 361, 1387
- [4] Booth, C. M., & Schaye, J. 2009, *MNRAS*, 398, 53
- [5] Bower, R. G., Morris, S. L., Bacon, R. et al. 2004, *MNRAS*, 351, 63
- [6] Chen, Y. M., Wang, J. M., Yan, C. Y., Hu, C., & Zhang, S. 2009, *ApJ*, 695, L130
- [7] Chevalier, R.A.1992, *ApJ*, 397, L39
- [8] Chevalier, R.A. & Clegg, A.W. 1985, *Nature*, 317, 44
- [9] Cid Fernandes, R., & Terlevich, R. 1995, *MNRAS*, 272, 423
- [10] Ciotti, L., & Ostriker, J. P. 2001, *ApJ*, 551, 131
- [11] Ciotti, L., Ostriker, J. P., & Proga, D. 2009, *ApJ*, 699, 89

- [12] Ciotti, L., Ostriker, J. P., & Proga, D. 2010, *ApJ*, 717, 708
- [13] Clarke, C. j., & Carswell, R. F. 2007, *Principles of Astrophysical Fluid Dynamics* (Cambridge Univ. Press)
- [14] Côté, P., et al. 2006, *ApJS*, 165, 57
- [15] Davies, R. I., Mueller Sánchez, F., Genzel, R., Tacconi, L. J., Hicks, E. K. S., & Friedrich, S. 2007, *ApJ*, 671, 1388
- [16] Davies, R., et al. 2010, *Co-Evolution of Central Black holes and Galaxies*, *Proceedings of the International Astronomical Union, IAU Symposium, Vol. 267*, p. 283
- [17] Dekel, A. & Silk, J. 1986, *ApJ*, 303, 39
- [18] Di Matteo, T., et al. 2005, *Nature*, 433, 604
- [19] Elmegreen, B. G. 1999, *ApJ*, 517, 103
- [20] Ferrarese, L., & Merritt, D. 2000, *ApJ*, 539, L9
- [21] Ferrarese, L., et al. 2006, *ApJ*, 644, 21
- [22] Ferreras, I., Scannapieco, E. & Silk, J. 2002, *ApJ* 579, 247
- [23] Filippenko, A. V., Ho, L. C. 2003, *ApJ*, 588, L13
- [24] Friaca, A. C. S. & Terlevich, R. J. 1998, *MNRAS*, 298, 399
- [25] Geyer, M. P. & Burkert, A. 2001, *MNRAS*, 323, 988

- [26] Gebhardt, K., et al. 2000, *ApJ*, 539, L13
- [27] González-Delgado, R. M., Cid Fernandes, R., Pérez, E., Martins, L. P., Storchi-Bergmann, T., Schmitt, H., Heckman, T., & Leitherer, C. 2004, *ApJ*, 605, 127
- [28] González-Delgado, R. M., Pérez, E., Cid Fernandes, R., & Schmitt, H. 2008, *AJ*, 135, 747
- [29] Graham, A. W., & Spitler, L. R. 2009, *MNRAS*, 397, 2148
- [30] Greve, T. R., Bertoldi, F., Smail, I. et al. 2005, *MNRAS*, 359, 1165
- [31] Hamann, F., & Ferland, G. 1999, *ARA&A*, 37, 487
- [32] Hao, C. N., Xia, X. Y., Mao, S. D., Deng, Z. G., & Wu, H. 2008, *CJAA*, Vol. 8, No. 1, 12
- [33] Hao, C. N., Xia, X. Y., Mao, S., Wu, H., & Deng, Z. G. 2005, *ApJ*, 625, 78
- [34] Heckman, T. M., Armus, L. & Miley, G. K. 1990, *ApJS*, 74, 833
- [35] Heckman, T. M. 2009, in *Astrophysics in the Next Decade, Astrophysics & Space Science Proceedings*, ed. H. A. Thronson, M. Stivelli, & A. Tiellens (Dordrecht: Springer), 335
- [36] Hobbs, A., Nayakshin, S., Power, C., & King, A. 2010, submitted (arXiv:1001.3883)

- [37] Holzer, T. E., & Axford, W. I. 1970, *ARA&A*, 8, 31H
- [38] Hueyotl-Zahuantitla, F., Tenorio-Tagle, G., Wünsch, R., Silich, S., & Palouš, J. 2010, *ApJ*, 716, 324
- [39] Hughes D. H., Serjeant, S., Dunlop, J. et al. 1998, *Nature*, 394, 241
- [40] Imanishi, M. 2003, *ApJ*, 599, 918
- [41] Jiménez-Bailon, E., Santos-Lleó, Mas-Hesse, J., Guainazzi, M., Colina, L., Cerviño, & González-Delgado, R. 2003. *ApJ*, 593, 127
- [42] Juárez, Y., Maiolino, R., Mujica, R. et al. 2009, *A&A*, 494, L25
- [43] King, A. 2003, *ApJ*, 596, 27
- [44] King, A. 2005, *ApJ*, 635, 121
- [45] Kormendy, J., & Bender, R. 2009, *ApJ*, 691, 142
- [46] Laird, E. S., Nandra, K., Pope, A., & Scott, D. 2010, *MNRAS*, 401, 2763
- [47] Lamers, H. J. G. L. M. & Cassinelli, J. P. *Introduction to Stellar Winds*, 1999, Cambridge University press, p. 62
- [48] Leitherer, C. & Heckman, T.M., 1995, *ApJS*, 96, 9
- [49] Leitherer, C., et al. 1999, *ApJS*, 123, 3

- [50] Leitherer, C., Schaerer, D., Goldader, J.D. et al., 1999, ApJS, 123, 3
- [51] Lipari, S. L., & Terlevich, R. J. 2006, MNRAS, 368,1001
- [52] Melioli, C. & de Gouveia Dal Pino, 2006, A&A, 445, L23
- [53] Meynet, G. & Maeder, A. 2002, A&A, 390, 561
- [54] Nesvadba, N. P. H., Lehnert, M. D., Genzel, R., et al. 2007, ApJ, 657, 725
- [55] Nulsen, P. E. J., & Fabian, A. C. 2000, MNRAS, 311, 346
- [56] Plewa, T. 1995, MNRAS, 275, 143
- [57] Rodriguez-Gonzalez, A., Canto, A., Esquivel, A., Raga, A. C. & Velazquez, P. F. MNRAS, 380, 1198
- [58] Rossa, J., van der Marel, R. P., Boker, T., Gersen, J., Ho, L. C., Rix, H.- W., Shields, J. C., & Walcher, C.-J. 2006, AJ, 132, 1074
- [59] Sarazin, C. L., & White, R. E., III.1987, ApJ, 320, 32
- [60] Scannapieco, E., Ferrara, A. & Madau, P. 2002, ApJ, 574, 590
- [61] Schartmann, M., Meisenheimer, K., Klahr, H., Camenzind, M., Wolf, S., & Henning, Th. 2009, MNRAS, 393, 759
- [62] Schinnerer, E., et al. 2008, ApJ, 689, L5

- [63] Seth, A., Agüeros, M., Lee, D., & Basu-Zych, A. 2008, *ApJ*, 678, 116
- [64] Silich, S., Tenorio-Tagle, G. & Añorve Zeferino, G.A. 2005, *ApJ*, 635, 1116
- [65] Silich, S., Tenorio-Tagle, G. & Hueyotl-Zahuantitla, F. 2008, *ApJ*, 686, 172
- [66] Silich, S., Tenorio-Tagle, G., Hueyotl-Zahuantitla, F., Palouš, J. & Wunsch, R. 2010, Co-Evolution of Central Black holes and Galaxies, Proceedings of the International Astronomical Union, IAU Symposium, Vol. 267, p. 336
- [67] Silich, S., Tenorio-Tagle G. & Muñoz-Tuñón, C. 2003, *ApJ*, 590, 796
- [68] Silich, S., Tenorio-Tagle G. & Muñoz-Tuñón, C. 2007, *ApJ*, 669, 952
- [69] Silich, S., Tenorio-Tagle, G., Muñoz-Tuñón, C., Hueyotl-Zahuantitla, F., Wunsch, R., & Palouš, J. 2010, *ApJ*, 711, 25
- [70] Silich, S., Tenorio-Tagle G. & Rodríguez González, A. 2004, *ApJ*, 610, 226
- [71] Silich, S., Tenorio-Tagle G., Torres-Campos, A., Muñoz-Tuñón, C., Monreal-Ibero, A. & Melo, V. 2009, *ApJ*, 700, 931

- [72] Silk, J., & Rees, M. J. 1998, *A&A*, 331, L1
- [73] Somerville, R. S., Hopkins, P. F., Cox, T. J., Robertson, B. E., & Hernquist, L. 2008, *MNRAS*, 391, 481
- [74] Stone, J. M. & Norman, M. L. 1992, *ApJS*, 80, 753
- [75] Strickland, D. K. & Heckman, T. M. 2009, *ApJ*, 697, 2030
- [76] Strickland, D. K. & Stevens, I. R. 2000, *MNRAS*, 314, 511
- [77] Swinbank, A. M., Chapman, S. C., Smail, I., Lindner, C., Borys, C., Blain, A. W., Ivison, R. J. & Lewis, G. F. 2006, *MNRAS*, 371, 465
- [78] Tacconi, L. J., Neri, R., Chapman, S. C. et al. 2006, *ApJ*, 640, 228
- [79] Tacconi, L. J., Genzel, R., Smail, I. et al. 2008, *ApJ*, 680, 246
- [80] Tenorio-Tagle, G. & Bodenheimer, P. 1988, *ARA&A* 26, 145
- [81] Tenorio-Tagle, G. & Muñoz-Tuñón, C. 1997, *ApJ*, 478, 134
- [82] Tenorio-Tagle, G. & Muñoz-Tuñón, C. 1998, *MNRAS*, 293, 299
- [83] Tenorio-Tagle, G., Muñoz-Tuñón, C., Pérez, E., Silich, S. & Telles, E. 2006, *ApJ*, 643, 186
- [84] Tenorio-Tagle, G., Silich, S. & Muñoz-Tuñón, C. 2003, *ApJ*, 597, 279

- [85] Tenorio-Tagle, G., Silich, S. Rodríguez González, A. & Muñoz-Tuñón, C. 2005, *ApJL*, 628, L13
- [86] Tenorio-Tagle, G., Wunsch, R., Silich, S. & Palouš, J. 2007, *ApJ*, 658, 1196
- [87] Terashima, Y., Iyomoto, N., Ho, L. C., & Ptak, A. 2002, *ApJS*, 139, 1
- [88] Tutukov, A. V., Shustov, B. M., & Wiebe, D. S. 2000, *Astron. Rep.*, 44, 711
- [89] Veilleux, S. Cecil, G. & Bland-Hawthorn, J. 2005, *ARA&A*, 43, 769
- [90] Wada, K., & Norman, C. A., 2002, *ApJL*, 566, L21
- [91] Walcher, C. J., Böker, T., Charlot, S., Ho, L., Rix, H.-W., Rossa, J., Shields, J. C., & van der Marel, R. P. 2006, *ApJ*, 649, 692
- [92] Walter, F., Riechers, D., Cox, P., Neri, R., Carilli, C., Bertoldi, F., Weiss, A., & Maiolino, R. 2009, *Nature*, 457, 699
- [93] Watabe, Y., Kawakatu, N., & Imanishi, M. 2008, *ApJ*, 677,895
- [94] Wehner, E. H., & Harris, W. E. 2006, *ApJ*, 644, L17
- [95] Wunsch, R., Tenorio-Tagle, G., Palouš, J. & Silich, S. 2008, *ApJ*, 683, 683

[96] Yuan, F., & De-Fu-Bu, MNRAS, 2010 (accepted)